Eur. Phys. J. C 49, 1117–1142 (2007)
DOI 10.1140/epjc/s10052-006-0193-3

THE EUROPEAN PHYSICAL JOURNAL C

Special Article – Tools for Experiment and Theory

C2GT: intercepting CERN neutrinos to Gran Sasso in the Gulf of Taranto to measure θ_{13}

A.E. Ball[1], A. Braem[1], L. Camilleri[1], A. Catinaccio[1], G. Chelkov[2], F. Dydak[1], A. Elagin[2], P.K. Frandsen[1], M. Gostkin[2], A. Grant[1], A. Guskov[2], C. Joram[1], Z. Krumshteyn[2], H. Müller[1], H. Postema[1], M. Price[1], T. Rovelli[3], D. Schinzel[1], J. Séguinot[4], G. Valenti[3], R. Voss[1,a], J. Wotschack[1], A. Zhemchugov[2]

[1] CERN, Geneva, Switzerland
[2] Joint Institute for Nuclear Research, Dubna, Russia
[3] Dipartimento di Fisica, Università degli Studi di Bologna and INFN, Bologna, Italy
[4] Institut de Physique Corpusculaire, Collége de France, Paris, France

Received: 8 April 2006 / Revised version: 13 June 2006 /
Published online: 2 February 2007 –

Abstract. Today's greatest challenge in accelerator-based neutrino physics is to measure the mixing angle θ_{13} which is known to be much smaller than the solar mixing angle θ_{12} and the atmospheric mixing angle θ_{23}. A non-zero value of the angle θ_{13} is a prerequisite for observing CP violation in neutrino mixing. In this paper, we discuss a deep-sea neutrino experiment with 1.5 Mt fiducial target mass in the Gulf of Taranto with the prime objective of measuring θ_{13}. The detector is exposed to the CERN neutrino beam to Gran Sasso in off-axis geometry. Monochromatic muon neutrinos of ≈ 800 MeV energy are the dominant beam component. Neutrinos are detected through quasi-elastic, charged-current reactions in sea water; electrons and muons are detected in a large-surface, ring-imaging Cherenkov detector. The profile of the seabed in the Gulf of Taranto allows for a moveable experiment at variable distances from CERN, starting at 1100 km. From the oscillatory pattern of the disappearance of muon neutrinos, the experiment will measure $\sin^2\theta_{23}$ and especially Δm^2_{23} with high precision. The appearance of electron neutrinos will be observed with a sensitivity to $P(\nu_\mu \to \nu_e)$ as small as 0.0035 (90% CL) and $\sin^2\theta_{13}$ as small as 0.0019 (90% CL; for a CP phase angle $\delta = 0^\circ$ and for normal neutrino mass hierarchy).

1 Introduction

The phenomenon of neutrino oscillations is experimentally established through deficits in the fluxes of atmospheric [1–8] and accelerator-produced [8–10] ν_μs, of reactor-produced [11, 12] $\overline{\nu}_e$s, of solar [13–24] ν_es, and through the satisfactory agreement with expectation of the solar neutrino flux inferred from charged-current (CC) and neutral-current (NC) reactions of solar neutrinos [21–24]. The experimental situation is complemented by a theoretical modelling in terms of the Maki–Nakagawa–Sakata (MNS) mixing matrix [25, 26] which relates three neutrino mass eigenstates to the three known flavour eigenstates.

The oscillations of neutrinos and their non-zero mass may well be the first indication of physics beyond the standard model. The current explanation of the smallness of neutrino masses is the see–saw mechanism in which the small masses of the left-handed neutrinos that we observe are the counterpart of very heavy right-handed neutrinos. The study of the neutrino mass spectrum should therefore give us some insight into this domain of masses which are inaccessible to present-day accelerators. Furthermore, contrasting this mass spectrum to that of quarks should help us understand fermion masses in general. If CP violation is observed in the neutrino sector, it could lead to an explanation for the matter–antimatter asymmetry of the universe.

After the phase of discovery and confirmation, the next step is the precise determination of the differences of the squares of the masses of the eigenstates (usually referred to as mass-squared differences) that determine the oscillation frequency, and of the four independent parameters of the MNS matrix. The measurement of the CP-violating phase angle δ stands out as the most important and difficult challenge. Prior to such a measurement, θ_{13} must be determined as precisely as possible because a non-zero value of θ_{13} is a prerequisite for observing CP violation in neutrino mixing.

The present paper discusses a project, called C2GT, to intercept the CERN neutrino beam to the Gran Sasso (CNGS) [27, 28], operated in unchanged geometry but at reduced neutrino energy, with an underwater Cherenkov detector in the Gulf of Taranto, with the prime objective of measuring θ_{13}.

Several other projects in Europe, the USA, and Japan are in progress or have been proposed to address the meas-

[a] e-mail: Rudiger.Voss@cern.ch

urement of θ_{13}, the mass hierarchy, and CP violation. They will be discussed in Sect. 8.

2 Physics motivation

The MNS matrix is a 3×3 unitary matrix which can be described as a product of three independent rotations governed by three mixing angles θ_{12}, θ_{13}, and θ_{23}, which link the triplet of mass eigenstates $[\nu_1,\,\nu_2,\,\nu_3]$ to the triplet of flavour eigenstates $[\nu_e,\,\nu_\mu,\,\nu_\tau]$. The MNS matrix incorporates a Dirac CP-violation phase δ (we ignore possible Majorana phases as they have no relevance for neutrino oscillations).

In the conventional parametrisation [25, 26], the MNS matrix U reads as follows:

$$U \equiv \begin{pmatrix} 1 & 0 & 0 \\ 0 & c_{23} & s_{23} \\ 0 & -s_{23} & c_{23} \end{pmatrix} \begin{pmatrix} c_{13} & 0 & s_{13}\mathrm{e}^{-\mathrm{i}\delta} \\ 0 & 1 & 0 \\ -s_{13}\mathrm{e}^{\mathrm{i}\delta} & 0 & c_{13} \end{pmatrix} \times \begin{pmatrix} c_{12} & s_{12} & 0 \\ -s_{12} & c_{12} & 0 \\ 0 & 0 & 1 \end{pmatrix}, \quad (1)$$

with $s_{12} \equiv \sin\theta_{12}$, and analogously for the other sines and cosines. In addition, for the three-neutrino case, two independent mass-squared differences Δm^2_{12} and Δm^2_{23} need to be specified.

The deficit of atmospheric neutrinos [1–8] is interpreted as oscillations of ν_μ into ν_τ from which θ_{23} and Δm^2_{23} can be extracted. In a 2-flavour analysis of Super-Kamiokande and K2K data [8], the 90% CL allowed range for these parameters is $\sin^2 2\theta_{23} > 0.93$ and $2.0 < \Delta m^2_{23} < 3.0\times10^{-3}\,\mathrm{eV}^2$ (since $|\Delta m^2_{12}| \ll |\Delta m^2_{23}|$, $\Delta m^2_{23} \cong \Delta m^2_{13}$).

The solar neutrino deficit is interpreted as an oscillation that depletes the original ν_e signal in favour of ν_μ and ν_τ from which θ_{12} and Δm^2_{12} can be extracted. The reactor $\overline{\nu}_e$ deficit is interpreted the same way. In a 3-flavour analysis [29], the recent results of SNO [21–24] and KamLAND [11, 12] in particular have constrained the corresponding oscillation parameters to allowed three-standard-deviation ranges of $0.24 < \sin^2\theta_{12} < 0.41$, and $7.0 < \Delta m^2_{12} < 9.3\times10^{-5}\,\mathrm{eV}^2$.

Only an upper limit is known for the angle θ_{13}. This has been set largely by the CHOOZ reactor experiment [30, 31]. In a 3-flavour analysis [29], the allowed three-standard-deviation range is $\sin^2\theta_{13} < 0.04$.

The above interpretations are based on the assumption that the LSND claim [32, 33] of a transition $\overline{\nu}_\mu \to \overline{\nu}_e$ with $\Delta m^2 \approx 1\,\mathrm{eV}^2$ does not stand up to verification. If it does, a fourth neutrino is needed which does not couple to the Z boson. Throughout the following, the point of view is taken that only the three known active neutrino flavours take part in neutrino oscillations.

Today's prime challenge in accelerator-based neutrino physics is the determination of the angle θ_{13}. The measurement of a finite value of the mixing angle θ_{13} is important per se but it would also open the door to a measurement of the CP-violating phase δ and of the mass hierarchy for which a future neutrino factory appears well suited. Two experiments are running or will start data-taking soon, but have a limited sensitivity to the appearance of ν_e in a ν_μ beam: MINOS may improve the CHOOZ limit on $\sin^2\theta_{13}$ by a factor of two [34]; OPERA will also improve the limit on $\sin^2\theta_{13}$ by a factor of two to three [35].

In the limit $|\Delta m^2_{12}| \ll |\Delta m^2_{23}|$, neutrino oscillation probabilities at planetary distances are well described by only three parameters: θ_{23}, $\Delta m^2_{23} \cong \Delta m^2_{13}$, and θ_{13}. The leading terms are [36]

$$\begin{aligned} P(\nu_e \leftrightarrow \nu_\mu) &\cong \sin^2\theta_{23}\,\sin^2 2\theta_{13}\,\sin^2\left(\frac{1.27\Delta m^2_{23}\,L}{E_\nu}\right), \\ P(\nu_e \leftrightarrow \nu_\tau) &\cong \cos^2\theta_{23}\,\sin^2 2\theta_{13}\,\sin^2\left(\frac{1.27\Delta m^2_{23}\,L}{E_\nu}\right), \\ P(\nu_\mu \leftrightarrow \nu_\tau) &\cong \cos^4\theta_{13}\,\sin^2 2\theta_{23}\,\sin^2\left(\frac{1.27\Delta m^2_{23}\,L}{E_\nu}\right), \end{aligned} \quad (2)$$

where the baseline L is measured in kilometres and the neutrino energy E_ν in GeV.

With nearly 'bi-maximal' mixing seemingly favoured by nature, with $\Delta m^2_{23} = 2.5\times10^{-3}\,\mathrm{eV}^2$ and with a small value of θ_{13}, (2) reduce to

$$\begin{aligned} P(\nu_e \leftrightarrow \nu_\mu) &\cong 2\sin^2\theta_{13}\,\sin^2\left(\frac{3.17\times10^{-3}L}{E_\nu}\right), \\ P(\nu_e \leftrightarrow \nu_\tau) &\cong 2\sin^2\theta_{13}\,\sin^2\left(\frac{3.17\times10^{-3}L}{E_\nu}\right), \\ P(\nu_\mu \leftrightarrow \nu_\tau) &\cong \sin^2\left(\frac{3.17\times10^{-3}L}{E_\nu}\right). \end{aligned} \quad (3)$$

Among the transitions in (3) the channels $\nu_e \leftrightarrow \nu_\mu$ and $\nu_e \leftrightarrow \nu_\tau$ are sensitive to θ_{13}. From the experimental point of view, the measurement of $\nu_e \to \nu_\mu$ or – equivalently, when ignoring CP violation – $\nu_\mu \to \nu_e$ oscillations is far superior to that of $\nu_e \to \nu_\tau$ oscillations, since the latter involves the detection of final-state taus for which a very fine-grained detector is needed. Before the ν_e beam of a future neutrino factory becomes available, a possible experiment is the search for the sub-leading $\nu_\mu \to \nu_e$ oscillation which could be present on top of the leading $\nu_\mu \to \nu_\tau$ oscillation, in a long-baseline experiment with a high-intensity ν_μ beam of conventional design.

From (3), both $\nu_\mu \to \nu_\tau$ and $\nu_\mu \to \nu_e$ oscillations have the first two maxima at $L \approx 400$ and 1200 km, for ν_μ of $E_\nu = 800\,\mathrm{MeV}$ and for $\Delta m^2_{23} = 2.5\times10^{-3}\,\mathrm{eV}^2$. The choice of energy is imposed by the geometrical layout of the CNGS beam discussed in Sect. 4. At these baseline lengths, the sensitivity to θ_{13} is maximal and the $\nu_\mu \to \nu_e$ transition probability takes the simple form

$$P(\nu_\mu \to \nu_e) \cong 2\sin^2\theta_{13}\,. \quad (4)$$

The precision of $\sin^2\theta_{13}$ is determined by the product of beam intensity and detector mass, on condition that the background can be kept sufficiently small.

Oscillations of type $\nu_\mu \to \nu_e$ are primarily sensitive to θ_{13}. However, they are also mildly sensitive to the mass hierarchy, the CP-violating phase δ, and to matter effects.

These dependencies must be taken into account when extracting a range of θ_{13} from a measurement of the $\nu_\mu \to \nu_e$ oscillation probability.

3 Principle of the experiment

The experiment is designed to detect near-monochromatic neutrinos of $E_\nu \approx 800\,\mathrm{MeV}$ from the CNGS beam in off-axis geometry, in an underwater Cherenkov detector in the Gulf of Taranto off the south coast of Italy. The trajectory of the beam above the Gulf of Taranto is shown in Fig. 1. A deep sea trench of a depth of at least 1000 m, which is the minimum depth required to shield optical detectors from daylight, starts only a few nautical miles off the coast near the northern tip of the gulf, such that the minimum baseline that can be used for an underwater experiment is about 1100 km. The trench extends several hundred kilometres into the Ionian Sea, remaining well aligned with the beam axis.

Muon and electron neutrinos are detected through quasi-elastic CC reactions in the sea water. For an incident neutrino energy of 800 MeV, muons and electrons will both radiate Cherenkov light over a distance $\leq 3.5\,\mathrm{m}$. The light is detected in a large planar detector built from a grid of optical elements and oriented such that the off-axis beam is oriented approximately normal to the detector plane. For tracks sufficiently far away from the detector plane, and with sufficient detector granularity, Cherenkov rings can be reconstructed. We assume a minimum distance between interaction vertex and detector of 10 m, and a detector granularity of $1.4 \times 1.4\,\mathrm{m}^2$.

The fiducial mass of the experiment is determined by the transverse size of the detector plane and by the light absorption in water which limits the useful longitudinal length. When we require that the Cherenkov rings be fully contained in the detector plane, the fiducial volume has the shape of a truncated cone, with a base diameter somewhat smaller than the transverse detector size. Further, we assume that we can detect Cherenkov rings for distances $10\,\mathrm{m} < z < 30\,\mathrm{m}$ from the interaction vertex to the detector. Therefore, the length of the fiducial volume is 20 m, equal to the height of the frustum of the cone. This corresponds to a fiducial mass of $\approx 1.5\,\mathrm{Mt}$.

The detector is built from discrete mechanical modules with dimensions $10 \times 10\,\mathrm{m}^2$. The detector thus consists of 30×30 mechanical modules which in turn accommodate

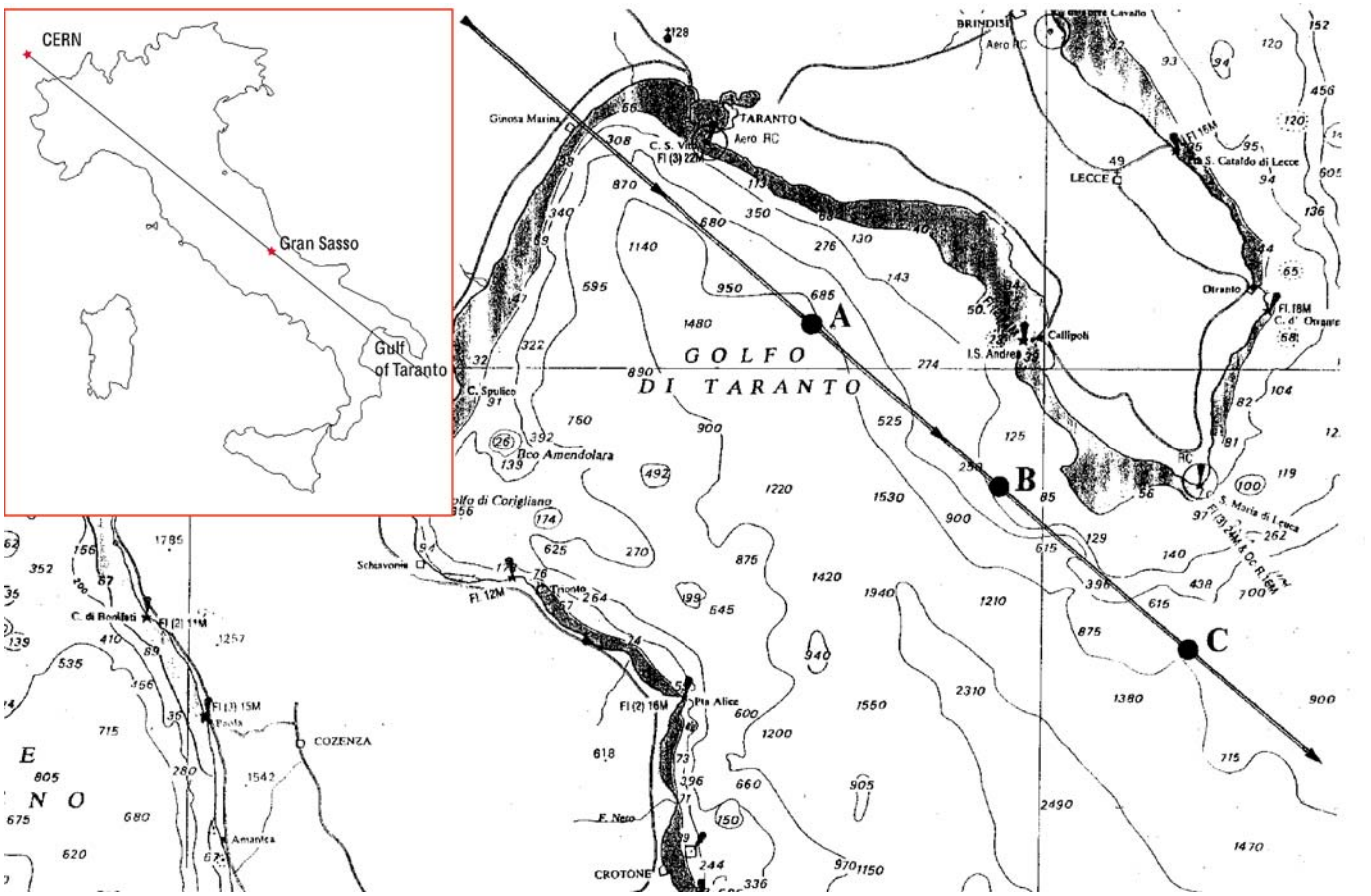

Fig. 1. Chart of the Gulf of Taranto. The axis of the CNGS is shown as a *solid line*. For orientation, the points A, B, and C show locations separated by 50 km, with B at a distance of 1200 km from CERN. In practice, the C2GT detector would be located slightly south-west of the line, i.e., at positions that are not exactly vertical below the beam axis

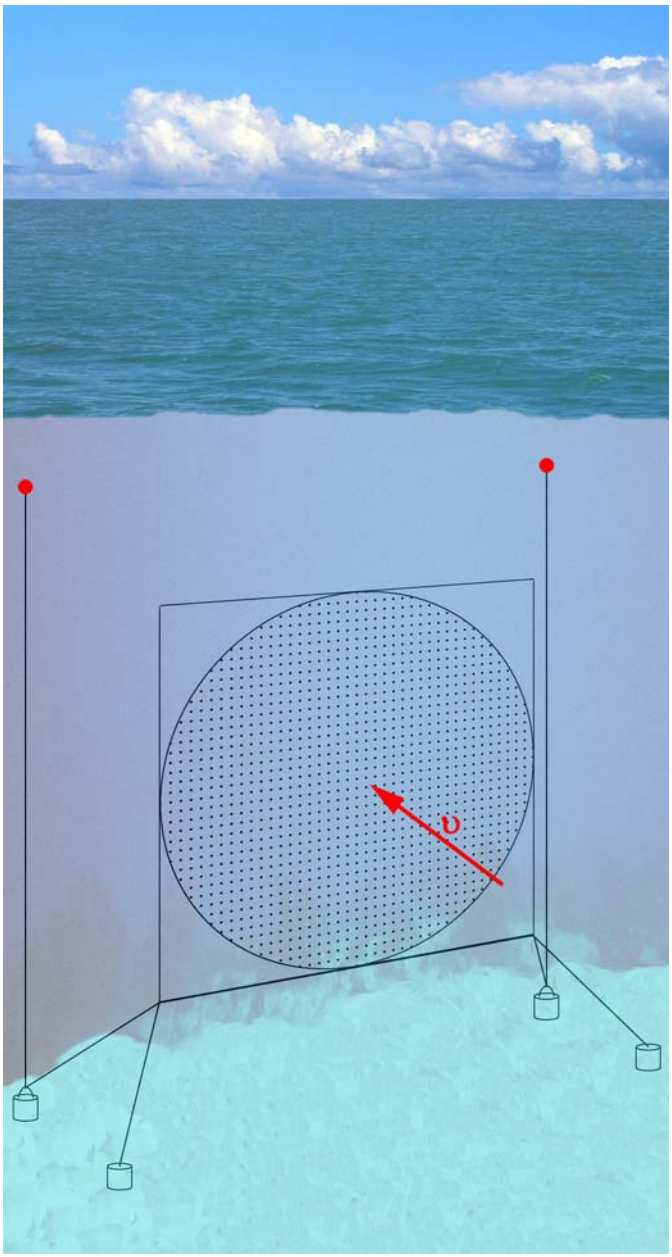

Fig. 2. Schematic view of the underwater detector (not to scale), including the lower mooring system. The upper mooring system, which completes the stabilization of the structure, is not shown

7×7 optical modules each. For reasons of economy, the instrumentation is limited to the largest circle that can be inscribed in the detector plane.

Figure 2 shows a schematic view of the underwater detector plane.

4 The neutrino beam

The difficulty of isolating a small signal of CC ν_e events from a potentially much larger background of NC events prevents the use of a conventional wide-band neutrino beam with its broad energy spectrum. Rather, a monochromatic neutrino beam is needed, which allows for an efficient suppression of NC events through their lower visible energy. At the same time, however, a high beam intensity is required which cannot be provided by a conventional narrow-band neutrino beam. These seemingly conflicting requirements are resolved by using a wide-band beam in off-axis geometry.

4.1 Beam characteristics in off-axis geometry

The concept of the off-axis geometry originated in 1993 at TRIUMF among a group of physicists who worked on what would evolve two years later into the E889 proposal to Brookhaven National Laboratory [37–39].

A conventional neutrino beam originates primarily from the decay of charged pions which travel along the axis of the neutrino beam. The longitudinal and transverse momenta of the ν_μ in the laboratory system are

$$p_{\mathrm{L}} = \gamma(p^* \cos\Theta^* + \beta p^*)\,,$$
$$p_{\mathrm{T}} = p^* \sin\Theta^*\,,$$

where β and γ are the Lorentz parameters, $p^* = 0.03\,\mathrm{GeV}/c$ is the neutrino momentum, and Θ^* is the polar angle of neutrino emission with respect to the pion direction of flight, all in the pion rest frame.

The polar angle Θ of neutrino emission in the laboratory frame is with $\beta \approx 1$

$$\Theta = \frac{R}{L} = \frac{1}{\gamma}\frac{\sin\Theta^*}{1+\cos\Theta^*}\,,$$

where R is the distance of the detector from the centre of the neutrino beam, and L the baseline.

It follows for neutrino emission perpendicular to the pion direction of flight in the pion rest frame ($\Theta^* = 90°$) that

$$\Theta = \frac{1}{\gamma}\,.$$

The neutrino energy as a function of the distance R from the beam centre is

$$E_\nu(R) = \frac{2\gamma p^*}{1+\left(\gamma\frac{R}{L}\right)^2}\,.$$

Therefore at the angle $\Theta = 1/\gamma$, E_ν is equal to half the energy at the beam centre.

The neutrino flux per unit area and per pion decay, as a function of the detector's distance from the beam centre, is

$$\Phi_\nu(R) = \frac{\frac{\gamma^2}{\pi L^2}}{\left(1+\left(\gamma\frac{R}{L}\right)^2\right)^2}$$

and has at the angle $\Theta = 1/\gamma$ one quarter of the intensity at the beam centre.

The most important kinematic property of the neutrino beam is that at the angle $\Theta = 1/\gamma$ the neutrino energy is in first approximation independent of the energy of the parent pion:

$$\frac{\partial E_\nu}{\partial \gamma} = 0\,.$$

Thus a nearly monoenergetic neutrino beam with high intensity is produced by a broad range of parent-pion momenta around the nominal momentum.

By contrast to ν_μ from pion decay, background neutrinos, e.g., from kaon decay do not obey the same kinematics and exhibit at the angle $\theta = 1/\gamma_\pi$ a broad energy spectrum.

Table 1 summarises the beam parameters for a detector location in the Gulf of Taranto, at a distance of 1200 km from CERN.

Figure 3 shows the dependence of the neutrino energy E_ν on γ_π at a distance of 1200 km from CERN and a distance of 44 km from the CNGS beam axis, i.e., at an off-axis angle $\theta = 1/27.1$ rad. The spectrum exhibits a broad maximum at $E_\nu \approx 800$ MeV. Therefore, a broad band of pion momenta between about 2 and 8 GeV/c contributes to the intensity of the nearly monoenergetic neutrino beam.

The low neutrino energy of ≈ 800 MeV is well below the threshold of ≈ 3.5 GeV for tau production on nucleons, so there is no background from such events despite the large $\nu_\mu \leftrightarrow \nu_\tau$ oscillation probability.

Table 1. Parameters of the neutrino beam and the detector location at a distance of 1200 km from CERN

Distance L from CERN	1200 km
Geodesic longitude	$17^\circ 54'$ E
Geodesic latitude	$39^\circ 47'$ N
Radial distance R from the CNGS beam axis	44 km
γ of parent pion	27.1
Nominal parent-pion momentum	3.8 GeV/c
Neutrino flux per decaying pion	4.1×10^{-15} cm^{-2}
Nominal neutrino energy from pion decay	0.81 GeV

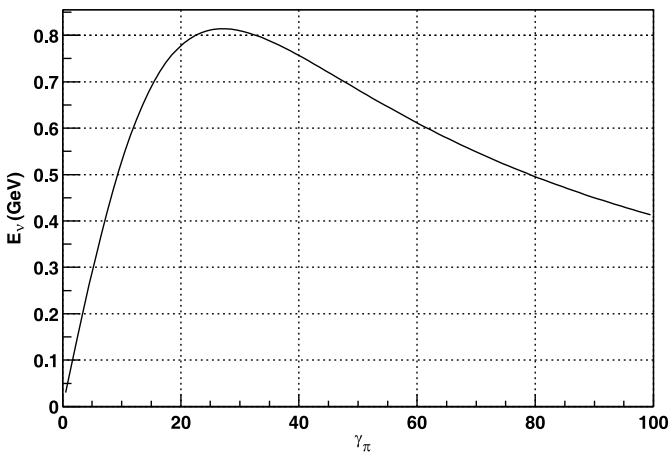

Fig. 3. Neutrino energy from pion decay as a function of γ_π at an off-axis angle $\theta = 1/27.1$

4.2 Target, horn, and reflector

For a high-sensitivity search for the appearance of ν_es, the highest possible number of π^+s with momentum around 4 GeV/c parallel to the beam axis is the prime requirement. Maximizing the number of pions requires a careful optimisation of the target length (for efficient transfer of the energy of the incoming proton to low-momentum pions) and of the target thickness (to help the escape of useful pions from the target).

The CNGS will be employed with unchanged geometrical layout and with unchanged incident proton momentum of 400 GeV/c . Only target, horn, and reflector need to be re-designed with a view to optimizing the flux of ≈ 4 GeV/c pions parallel to the beam axis.

Figure 4 shows the results of a FLUKA study of the combined yield of π^+s and π^-s from the interactions of 400 GeV/c protons in rotationally symmetric graphite targets with different absorption lengths and radii. It appears that a target of four absorption lengths (152 cm) and a radius of 2.5 mm is optimal.

The main device for focusing the pions to an angle of less than a few milliradians with respect to the beam axis is a magnetic horn. Its design must respect practical constraints: outer radius not exceeding 0.75 m, length not exceeding 6.65 m, and current not exceeding 150 kA for reliable long-term operation. The yield of useful π^+s is further improved by a reflector installed ≈ 50 m downstream of the target–horn system. The reflector must respect the same

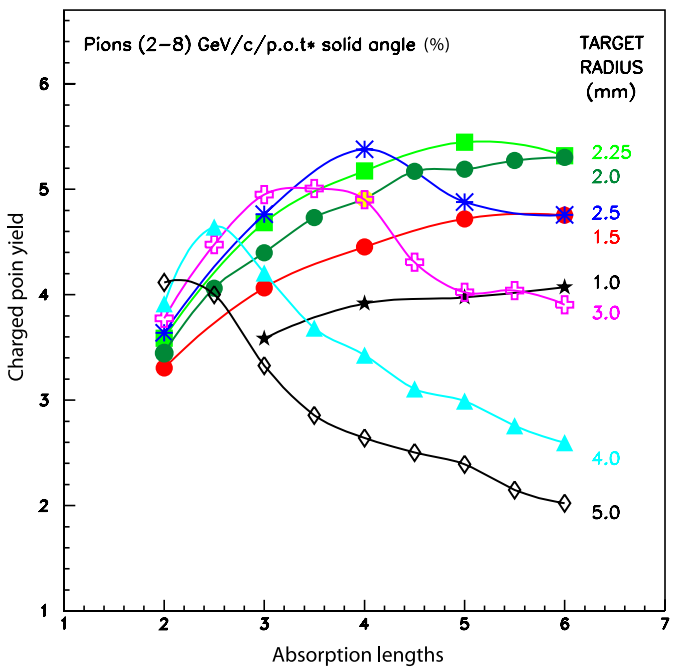

Fig. 4. Yield of $\pi^\pm$'s from rotationally symmetric graphite targets with different absorption lengths and radii

Table 2. Parameters of target, horn, and reflector

Target	Material	graphite
	Length	1.52 cm ($4\lambda_{\rm abs}$)
	Radius	2.5 mm
	Location	0–1.52 m
Horn	Length	6.65 m
	Radius (max.)	0.75 m
	Current (pulsed)	150 kA
	Location	0.65–7.30 m
Reflector	Length	6.65 m
	Radius (max.)	0.75 m
	Current (pulsed)	180 kA
	Location	50.00–56.65 m

geometrical constraints as the horn, but it can be operated reliably with a current up to 180 kA.

With a view to maximizing the flux of π^+s around the nominal momentum of $\approx 4\,{\rm GeV}/c$, the optimum shapes of horn and reflector were determined, together with their respective distances to the target. Table 2 lists the salient parameters of the system of target, horn, and reflector. The longitudinal profiles of the horn and the reflector are shown in Fig. 5.

The combined focusing by horn and reflector amplifies the useful π^+ flux by a factor of ≈ 120, where the reflector contributes a factor of ≈ 1.75. There are $\approx 0.7\pi^+$ per proton incident on the target that contribute to the useful ν_μ flux.

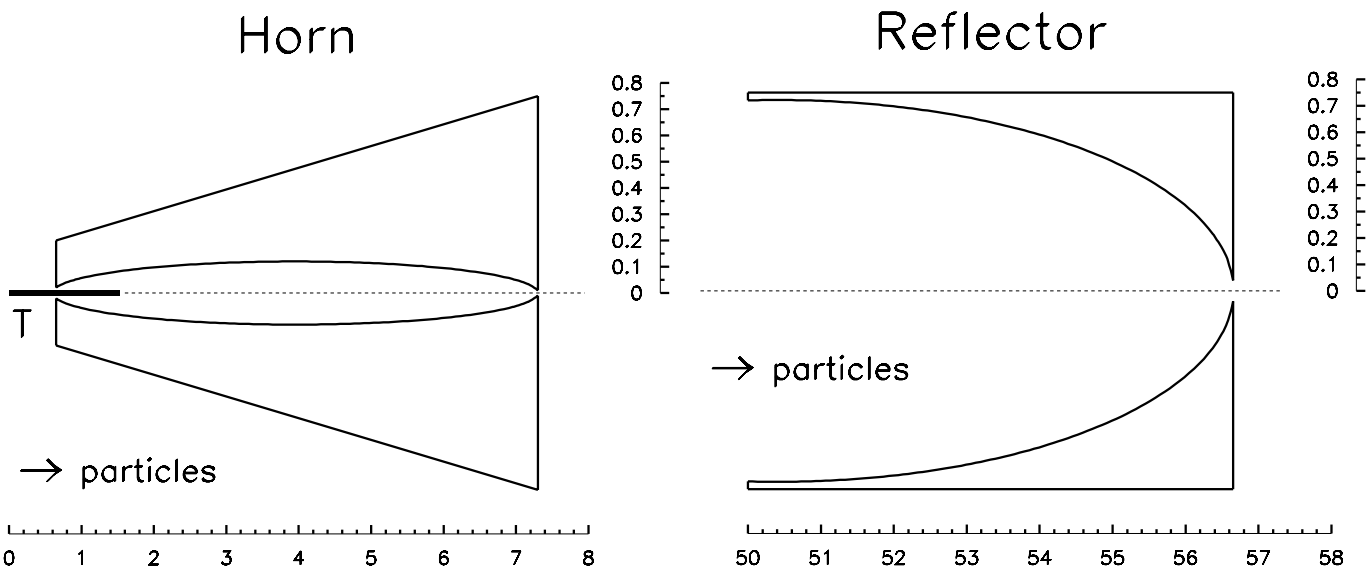

Fig. 5. Longitudinal profiles of the horn (*left*) and the reflector (*right*). The location of the target T with respect to the horn is also shown. All scales are in m

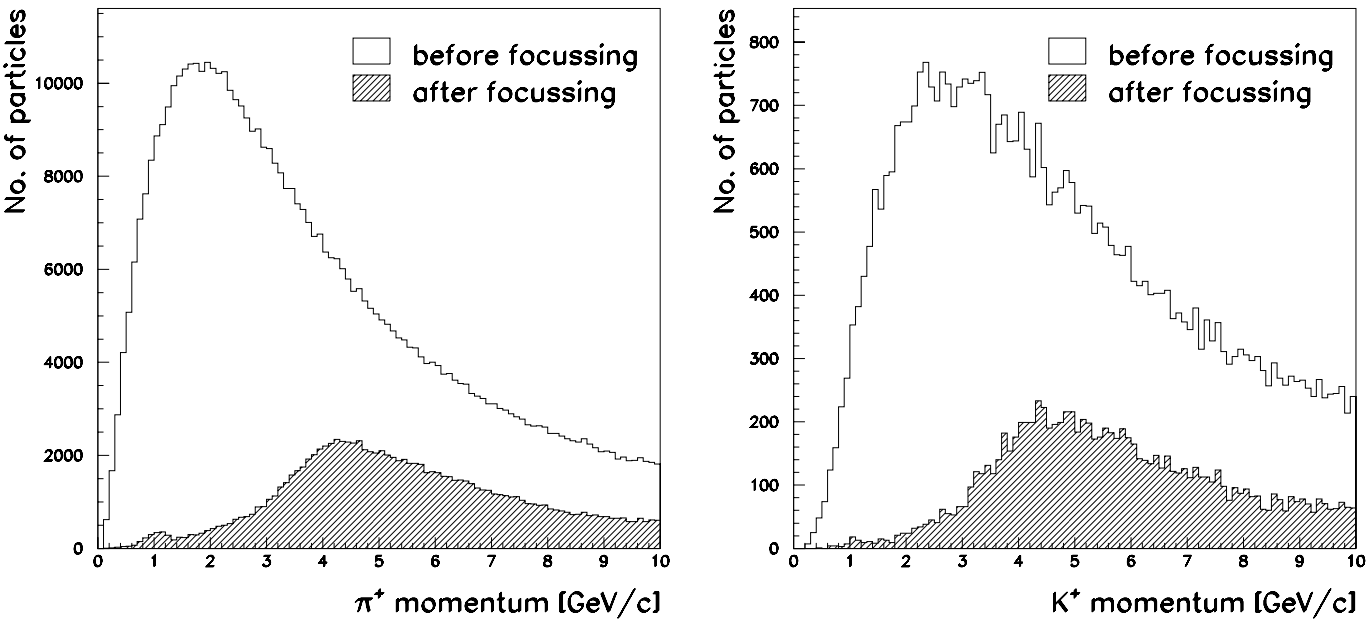

Fig. 6. Momentum spectra of π^+'s (*left*) and K^+'s (*right*) before and after horn and reflector focusing

The resulting spectra of π^+s and K^+s before and after the focusing by horn and reflector are shown in Fig. 6. The selective focusing with a most probable π^+ momentum slightly above 4 GeV/c is apparent. With a view to exploiting the peculiar dependence of the neutrino energy on the π^+ momentum shown in Fig. 3, the focusing is designed so as to favour momenta above rather than below 4 GeV/c.

4.3 Neutrino event spectra

The decay of the focused $\pi^{\pm}$s and $K^{\pm}$s in the evacuated decay tunnel of the CNGS with 1000 m length and 2.45 m diameter has been simulated, resulting in normalised flux and event spectra of various neutrino species. For the plots and tables presented in this section, the cross-sections shown in Fig. 17 and listed in Table 6 (Sect. 7.1)

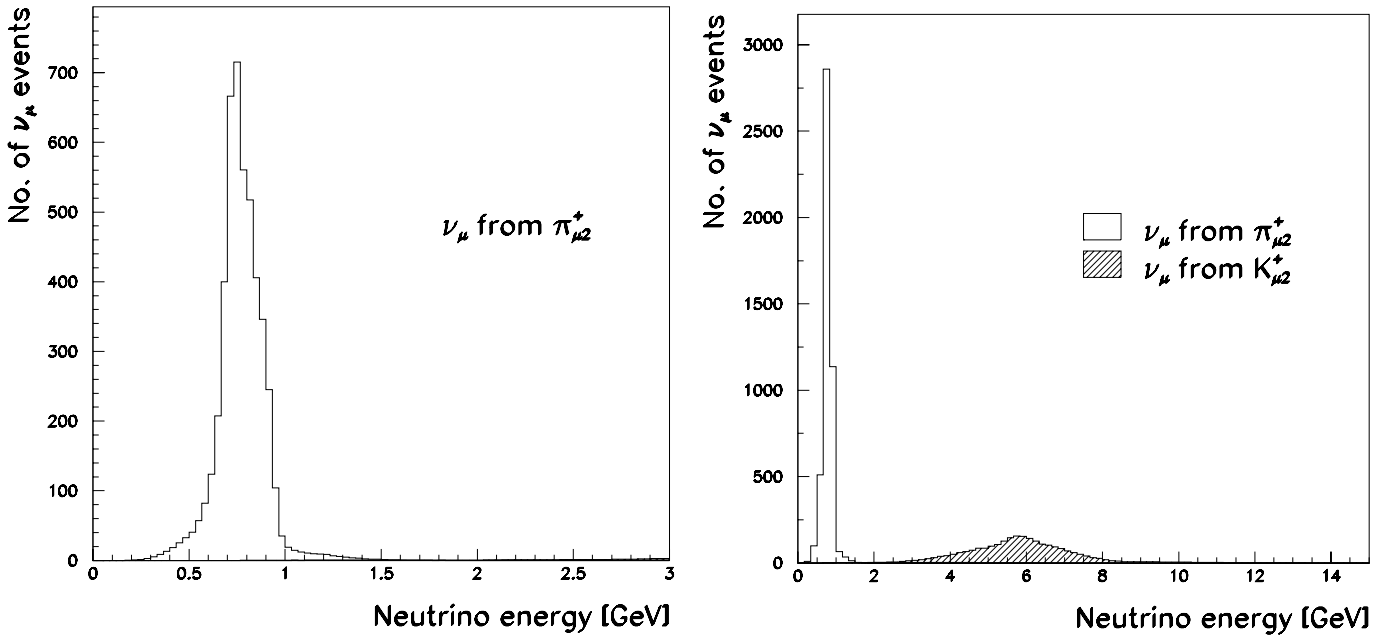

Fig. 7. Momentum spectra (before oscillations) of ν_μ events from π^+ and K^+ decays. The *left plot* shows the momentum spectrum of ν_μ events from π^+ decays in more detail; the ν_μ events from K^+ decays are hardly visible on this scale

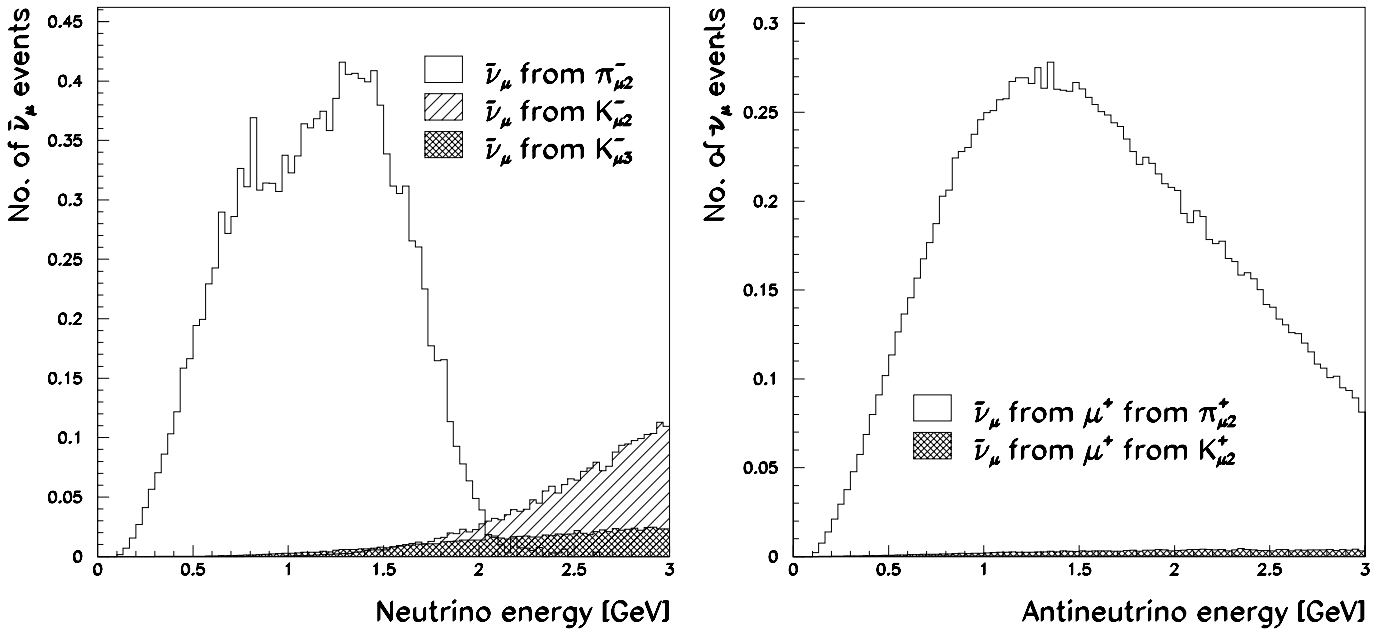

Fig. 8. Momentum spectra (before oscillations) of $\overline{\nu}_\mu$ events from π^- and K^- decays (*left*), and of $\overline{\nu}_\mu$ events from μ^+'s originating from π^+ and K^+ decays (*right*). $\overline{\nu}_\mu$ events from μ^+'s originating from $K^+_{\mu 3}$ decays are not shown because they would be hardly visible on this scale

were used. The event numbers refer to a 1.5 Mt detector located 1200 km from CERN in the Gulf of Taranto, for an exposure of 25×10^{19} protons of 400 GeV/c on target, corresponding to five years of operation.

Figure 7 shows the spectra of the ν_μ events from the decays of π^+s and K^+s. Neutrino oscillations are assumed to be absent. The nearly monochromatic line of ≈ 800 MeV ν_μs from pion decay is apparent which stems from the off-axis geometry.

The focusing strongly favours positively charged hadrons and disfavours negatively charged hadrons; yet a few negatively charged hadrons survive. The $\overline{\nu}_\mu$ events from π^- and K^- decays are shown in the left plot of Fig. 8. At ≈ 800 MeV, the contamination of $\overline{\nu}_\mu$ events is 0.14%. A second, comparable, source of $\overline{\nu}_\mu$s are μ^+s from the decay of π^+s and K^+s. The resulting spectra are shown in the right plot of Fig. 8. Since the detector is non-magnetic and the signal is made of quasi-elastic events, antineutrino events are not background but are part of the signal.

A dangerous background arises from the flux of genuine ν_es of which there are two main sources. The first source is ν_es from K^+_{e3} decays, the other is ν_es from the decay of μ^+s from π^+ and K^+ decays. The event spectra from these sources are shown in Fig. 9. It appears that at ≈ 800 MeV, the events from the decay of μ^+s originating from π^+s are dominant. This is an unfortunate consequence of the fact that the 1000 m decay tunnel is much longer than necessary and has not been optimised for the experiment discussed here. For example, with a 300 m decay tunnel, the number of signal events would be reduced by 16%, however, the background of genuine ν_e events would be reduced by almost a factor of two from ≈ 10.3 to ≈ 6 events.

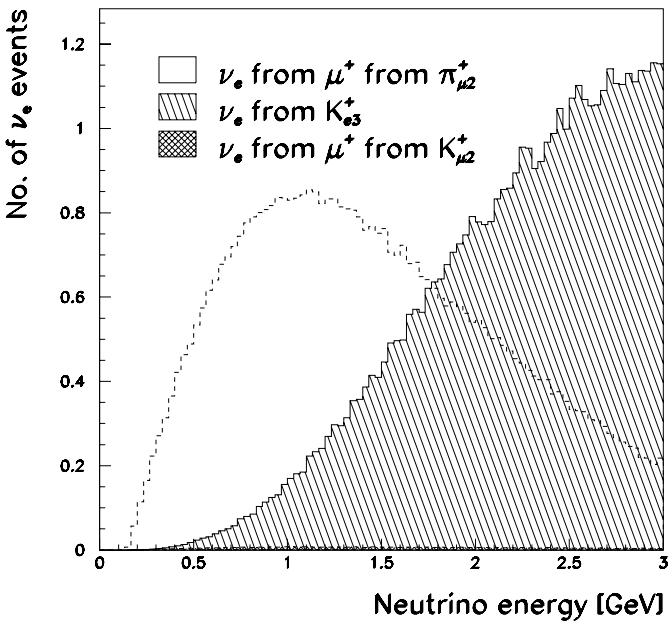

Fig. 9. Momentum spectrum (before oscillations) of ν_e events from K^+_{e3} decays, and from the decays of μ^+'s originating from π^+ and K^+ decays (*bottom*); ν_e events from μ^+'s originating from K^+_{e3} decays are hardly visible on this scale

Table 3. Number of neutrino events (before oscillations) expected in a 5-year exposure in a 1.5 Mt detector in the Gulf of Taranto, for all energies and for the 'signal region' 0.6 GeV $< E_\nu^{\rm vis} <$ 1.0 GeV

Parent hadron decays	Neutrino type	All	0.6–1.0 GeV
$\pi^+_{\mu 2}$	ν_μ	4731	4327
	$\overline{\nu}_\mu$ from μ^+	16.8	2.4
	ν_e from μ^+	50.5	9.1
$K^+_{\mu 2}$	ν_μ	2488	0.17
	$\overline{\nu}_\mu$ from μ^+	0.42	0.018
	ν_e from μ^+	0.69	0.079
$K^+_{\mu 3}$	ν_μ	71.7	0.72
	$\overline{\nu}_\mu$ from μ^+	0.024	0.0032
	ν_e from μ^+	0.068	0.017
K^+_{e3}	ν_e	107	1.1
$\pi^-_{\mu 2}$	$\overline{\nu}_\mu$	13.9	3.7
	ν_μ from μ^-	0.11	0.0091
	$\overline{\nu}_e$ from μ^-	0.014	0.0027
$K^-_{\mu 2}$	$\overline{\nu}_\mu$	127	0.0012
	ν_μ from μ^-	0.065	0.0045
	$\overline{\nu}_e$ from μ^-	0.022	0.0014
$K^-_{\mu 3}$	$\overline{\nu}_\mu$	3.4	0.017
	ν_μ from μ^-	0.0042	0.00054
	$\overline{\nu}_e$ from μ^-	0.0019	0.00017
K^-_{e3}	$\overline{\nu}_e$	5.1	0.024

Table 3 summarises the event numbers (before oscillations) expected from various neutrino species from the most important $\pi^\pm$ and $K^\pm$ decay channels.

5 Environmental conditions in the Gulf of Taranto

The Gulf of Taranto is somewhat sheltered against the open sea and is far from the rivers Rhône, Po, and Nile, which are the three main sources of pollution of the Mediterranean. Therefore one can expect good oceanographic conditions for the C2GT experiment, although we have no on-site data that support this expectation. Rather, we rely on the experience from the NEMO and NESTOR Collaborations [40–42] whose sites at Capo Passero (Sicily) and Pylos (Greece) are some 400 km farther to the south-west and south-east, respectively.

5.1 Wind, waves, and currents

In the decade from 1992 to 2002, the maximum observed wind speed in the centre of the Gulf of Taranto was 16 m/s, and the maximum wave height from crest to trough was 5–6 m, where this wave height is defined as the average of the highest one-third of all wave heights. That implies that one might encounter within a three-hour period (equivalent to 1000 waves) one wave that might reach 10 m from crest to trough [43, 44].

Water currents are an issue because of their impact on the design of the mechanical structure of the detector. Weak and steady water currents are also preferable since they seem to excite less bioluminescence than strong water currents. Fortunately, the sea bed of the Gulf of Taranto is rather smooth, with no canyons that may lead to turbulent water currents.

The NEMO Collaboration measured the water currents at their Capo Passero site over 36 months. The currents proved rather stable in direction and velocity. The typical velocity was 3 cm/s at a depth of ≈ 3000 m, with a maximum value of 10 cm/s [40–42].

5.2 Organic and inorganic particulates

The presence of organic and inorganic particulates in the sea water affects detector performance because of changes in the scattering and absorption of Cherenkov light. Sedimentation on the optical modules and the growth of bacterial films or the settling of marine micro-organisms ('biofouling') on the optical modules will degrade light transmission and thus reduce detection efficiency and, eventually, limit the operational lifetime.

The Ionian sea, of which the Gulf of Taranto is part, has a low bacterial concentration, which reduces biofouling and optical noise from bioluminescence [40–42].

The NEMO Collaboration reported a typical sedimentation rate of 20 mg/m^2 day at their Capo Passero site which is believed to permit the operation of upward-looking optical detectors for at least one year. The NESTOR Collaboration reported an even lower sedimentation rate at their Pylos site so that they consider the operation of upward-looking optical detectors over many years quite possible.

5.3 Light transmission in sea water and impact on detector design

The intensity of Cherenkov photons is proportional to $1/\lambda^2$, where λ is the photon wavelength. This spectrum is heavily distorted by the absorption properties of sea water, which is different from the absorption in fresh water because of the salt content. The absorption length used in our simulations is the one measured by the ANTARES collaboration [45] and is shown in Fig. 10.

The spectrum of Cherenkov photons will be different for different distances in sea water. For a typical distance of 20 m, the resulting spectrum is well matched to the typical quantum efficiency of bi-alkali photocathodes.[1] An example is shown in Fig. 11.

For photon scattering, we adopted the procedures which are used by the ANTARES Collaboration [45]. Each

[1] We adopted the typical spectral response of the photomultiplier tube R1828-01 from HAMAMATSU.

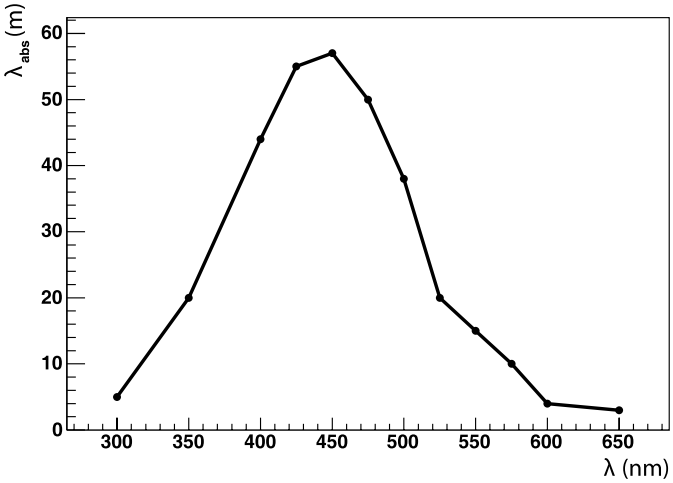

Fig. 10. Light absorption length in sea water as a function of wavelength

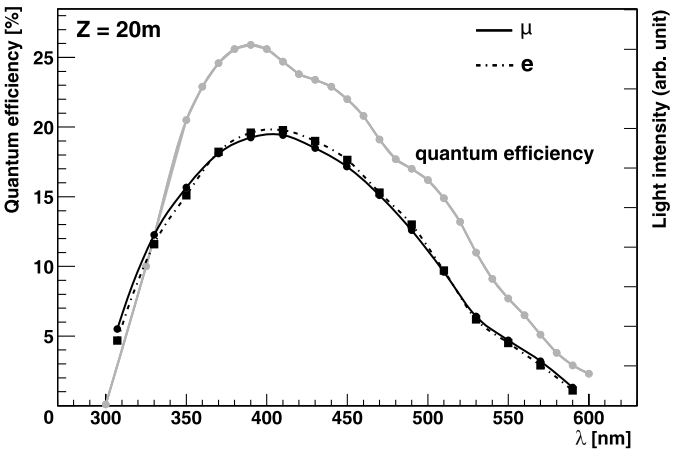

Fig. 11. Cherenkov light intensity (arbitrary units), as a function of wavelength after absorption in 20 m of sea water (*full* and *dotted black lines*); the typical quantum efficiency of a bi-alkali photocathode in per cent is shown as a *grey line*

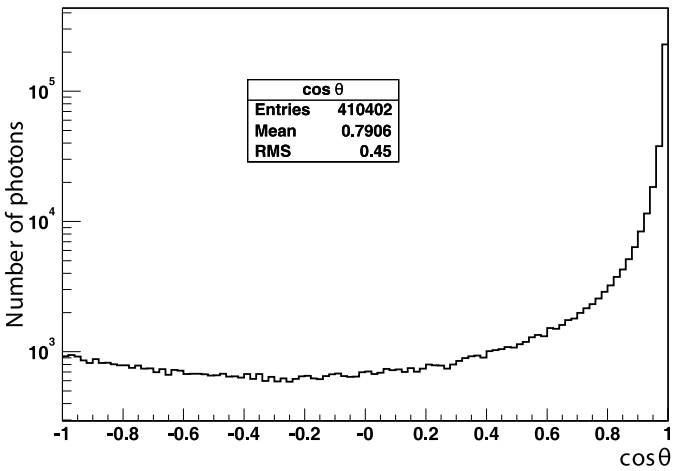

Fig. 12. The cosine of photon scattering angle in sea water, showing the superposition of forward–backward symmetric Raleigh scattering and forward Mie scattering

photon can undergo Mie scattering and Raleigh scattering, where Mie scattering occurs with a probability of 86%. The distribution of scattered photons is dominant in the forward direction for Mie scattering, but forward–backward symmetric for Raleigh scattering. The resulting overall distribution of scattering angles is shown in Fig. 12.

The last ingredient is the photon scattering length in sea water. Again following ANTARES, we adopted a linear parametrisation of measurements at wavelengths $\lambda = 375$ and 475 nm: $\lambda_{\rm scatt} = 53 + 0.265(\lambda - 475)$. The scattering length at $\lambda = 475$ nm is therefore $\lambda_{\rm scatt} = 53$ m.

6 The neutrino detector

Although a large number of Cherenkov photons are generated, there is a rapid fall-off of the number of photons with distance due to absorption in water, so that only a few photoelectrons would be produced in a photo-detector with an area of $\approx 1\,{\rm m}^2$. Therefore in our first designs of the detector, the light collecting efficiency was augmented by the use of rotationally symmetric parabolic mirrors, optimised for the collection of light under the Cherenkov angle of incidence (42°). It was realised, however, that the angular response function of such mirrors was too strong a function of the angle of incidence of the Cherenkov light with respect to the mirror axis (Fig. 13): certain signatures of the events, such as the 'fuzziness' of rings produced by electrons, would be degraded; even more seriously, in the case of a $\pi^0 \to 2\gamma$ decay there is a chance of missing one of the rings completely. Hence the mirror concept was abandoned in favour of optical modules with a much flatter angular response function.

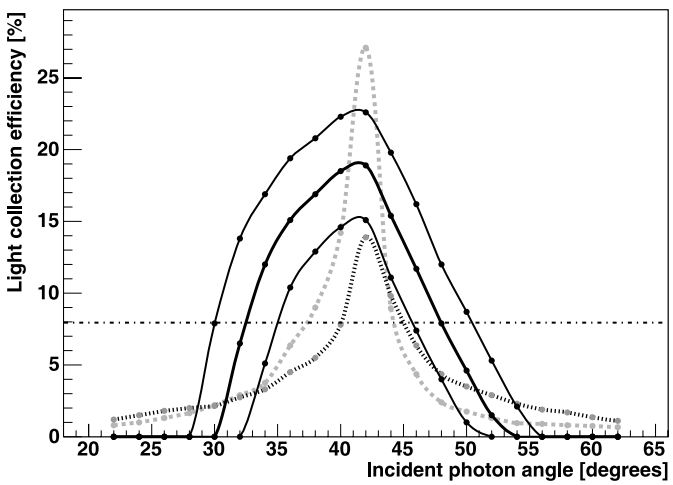

Fig. 13. Angular response functions: the three *continuous lines* show the light collection efficiency of a parabolic mirror system with photodetectors with diameter 40, 50, and 60 cm, respectively; the *horizontal line* shows the geometrical light collection efficiency of 8% that was used in our simulations. For comparison, the angular incidences of photons from perpendicularly incident 800 MeV electrons (*dotted*, *dark*) and muons (*dotted, light*) are also shown

We also considered a different detector type based on photon conversion in wavelength-shifting fibres. That was motivated by the abundance of UV photons in Cherenkov radiation. However, that concept proved not feasible since the salt in sea water makes it opaque for UV photons.

Our simulations use the measured light transmission in the Mediterranean Sea and the quantum efficiency of bi-alkali photo-cathodes (both as a function of wavelength). These simulations indicate that, if the photo-sensitive area is at least $\approx 4\%$ of the surface area of the detector plane seen by the Cherenkov photons, the experiment is feasible.

6.1 The optical module

The design of the optical module is driven by the scientific requirements and the special environmental conditions:

- efficient light detection in the wavelength range 300–550 nm;
- maximal surface and angular acceptance;
- sensitivity to a single photoelectron;
- timing resolution ≤ 2 ns;
- random background of ≤ 1 MHz;
- operation in sea water at a depth of ≈ 1000 m.

In view of these specifications and of cost considerations, we embarked on a new concept of an optical module. It consists of a large, almost spherical, hybrid photon detector (HPD), inserted in a spherical glass container which withstands high pressure. We have chosen the HPD technology [46] rather than a conventional photomultiplier tube, because it provides good signal characteristics with single photoelectron counting ability and uniform collection efficiency also for large angles of photon incidence.

Since the HPD's sensitivity is by design independent of the angle of photon incidence, the geometrical light collection efficiency is not flat but increases with angle of incidence. Taking into account the increase at the Cherenkov angle, we need one optical module every 1.4 m on a square grid to achieve a geometrical light collection efficiency of $\approx 8\%$. This granularity requires a total of 32 000 optical modules.

Exploiting experience in the design and construction of high-performance HPDs [47], we are building a prototype HPD of the above type with an outer diameter of 210 mm,[2] with the aim of verifying the HPD characteristics.

6.1.1 Design characteristics of the hybrid photon detector

The HPD design is schematically shown in the left part of Fig. 14, while a photograph of a half-size prototype of the HPD is shown in the figure's right part.

Mechanically, the HPD is based on a spherical envelope of borosilicate glass of 380 mm outer diameter and wall thickness of 5 mm. The bottom part of the glass envelope is sealed by a metallic baseplate equipped with electrical feedthroughs. A semi-transparent bi-alkali photocathode covers the inner glass surface down to the shaper electrode.

[2] We wish to acknowledge the cooperation with PHOTONIS SAS, Brive-la-Gaillarde, France, in this R and D project.

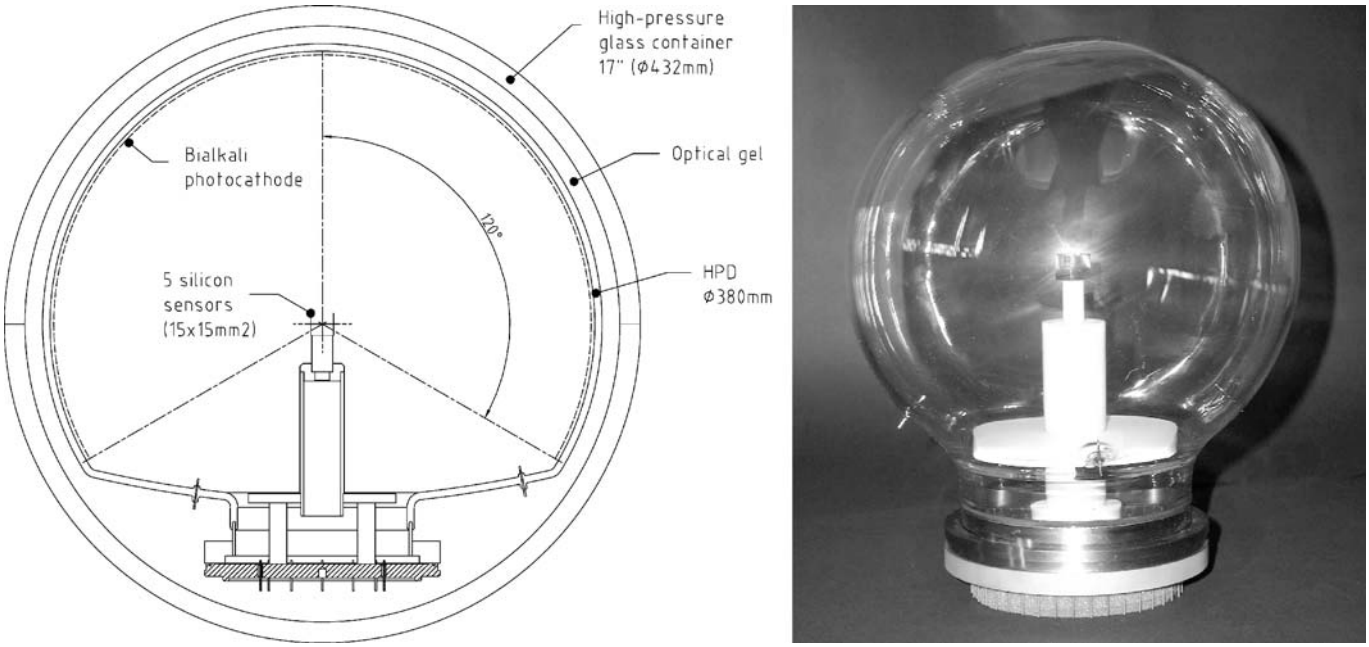

Fig. 14. Schematic view of the optical module (*left*); photograph of a half-size prototype of the HPD (*right*)

The photocathode is held at a negative high voltage of 20 kV, while the silicon anode is grounded.

The photoelectrons are accelerated in the radial electric field between the cathode and the silicon anode. Electrostatic simulations predict a uniform angular acceptance within $\approx 110°$ with respect to the HPD axis, with a transit time spread below 1 ns and insensitivity to the Earth's magnetic field.

The HPD is housed in a standardised high-pressure glass container as used by the fishing industry. The 380 mm HPD fits in a 17-inch container with a gap of 1 cm. The optical and mechanical contact between the HPD and the container is ensured by an optical gel with matched refractive index. Underneath the HPD, where the container is equipped with industrial pressure and sea-water-proof feedthroughs, sufficient space for a HV supply and calibration electronics is available.

The HPD's silicon anode consists of 20 silicon diodes with 20 pF capacity each, which are located on five faces of a cube-shaped ceramic anode of $15 \times 15 \times 15\,\mathrm{mm}^3$ volume. Each face is segmented into four diodes. The sixth, bottom, face of the cube sits on an insulated cylinder which in turn is mounted on the baseplate. The cube is surrounded by a field cage of about 30 mm diameter, which is largely transparent to the photoelectrons. Its role is to reduce the electric field gradient in the vicinity of the silicon sensor to values which exclude electric discharges from the silicon surfaces.

6.1.2 Frontend electronics characteristics

Single photoelectrons produce about 4500 electron–hole pairs in the active part of the silicon diodes. The small signal of ≈ 0.7 fC per photoelectron is converted by a charge-sensitive preamplifier into a voltage swing of 1 mV/fC and is then shaped further.

In most cases the signal will be detected by a single silicon diode, since charge sharing between adjacent diodes is nearly negligible. The probability that a 20 keV photoelectron is backscattered from the silicon diode, is about 18%. Because of the partial energy deposition, an almost flat tail develops in the charge spectrum that extends from the one-photoelectron peak down to zero. To minimise the impact of backscattering on the detection efficiency, a signal-to-noise ratio as high as possible is desirable. Assuming a 4σ noise cut, a signal-to-noise ratio of 10 (i.e., an r.m.s. noise of ≤ 500 electrons) maintains the detection efficiency at 93%.

With an overall 25 pF capacitance per silicon diode (which includes 5 pF from the preamplifier) and the noise increasing with the square of the capacitance, this signal-to-noise ratio requires a large shaping time and lowest possible $1/f$ noise. With a worst-case noise rate of 1 MHz per HPD (consistent with the background of 0.1 photoelectrons per event and the $2.8 \times 2.8\,\mathrm{m}^2$ area that has been assumed in the event generation and reconstruction; see Sect. 7.2) signals can be well discerned from noise if the signal peaking time is smaller by at least a factor of three than the average time delay between noise signals. Since the signal peaking time of a second-order shaper is twice the shaper time constant, the latter is 150 ns for a peaking time of ≈ 300 ns. The requirement for a timing resolution of less than 2 ns is compatible with that peaking time if the shaper yields a gamma-function-compliant pulse shape with amplitude-independent time reference points for offline evaluation. With the sampling frequency derived from the CERN-SPS clock of 40.0792 MHz (Sect. 6.2.1), the signal can be sampled above the minimum Nyquist frequency of ≈ 7 MHz by applying downscaling factors of 1/1, 1/2, or 1/4.

The desired r.m.s. noise level of ≤ 500 electrons requires for a 150 ns shaper time constant less than ≈ 20 electrons/pF, which seems achievable.

Table 4. Characteristics of the frontend electronics

Overall channel capacitance	25 pF
Single photoelectron signal	$\approx 4500\,e$
Shaping time	150 ns
r.m.s. noise	$\leq 500\,e$
Maximum sampling frequency	40.0792 MHz
Dynamic range	6 photoelectrons

The dynamic range of six photoelectrons is accommodated by an 8-bit FADC by placing the least significant bit at the noise level.

The characteristics of the HPD frontend electronics are summarised in Table 4.

6.2 Readout, data acquisition, monitoring and calibration

6.2.1 Electronics readout and data acquisition

The global strategy of data readout is driven by the spill structure of the CERN-SPS: the accelerator is assumed to operate with two fast spills, each of $\approx 10\,\mu$s length and separated by a 50 ms spill pause. By storing all FADC samples from each optical module during the two successive spills, both light signals and noise are continuously recorded. That renders an 'event trigger' superfluous and eliminates questions of trigger efficiency. We call this ensemble of data a 'physics event'.

The correct timing of the spill gates is achieved in the following way. At each start of a magnet cycle of the SPS an encoded signal specifying the accelerator cycle number is sent via satellite to the Gulf of Taranto. Since the elapsed time between the start of the magnet cycle and the extraction is fixed, precise setting of the two gates for data recording can be achieved by using two equal GPS-disciplined clocks oscillating at the clock frequency of the CERN-SPS. One clock is used at CERN as reference clock, while the other is used as master clock at the experiment. The cycle number then determines the opening time of the gates for data recording.

The data of an event are transferred into the memory of the main DAQ computer on the surface, using Gigabit Ethernet technology over fibre optics.

The 900 mechanical modules of the C2GT detector form, in principle, a matrix of 30 columns and 30 rows. For simplicity, we discuss here the electronics readout and data acquisition of the full square of 30 columns and 30 rows, whereas in practice the instrumentation will be limited to the area within the largest inscribed circle.

Each mechanical module consists of 49 optical modules forming a 7×7 matrix. Each optical module delivers 20 signals from its silicon diodes. Their readout is organised in 30 parallel branches corresponding to the 30 columns of the detector.

The master clock's signal is distributed via optical fibres to the centre of each mechanical module. From there it is fanned out to the 49 optical modules.

Table 5. Number of readout channels, data volume and transfer times

Total number of optical modules	44 100
Total number of readout channels	882 000
Number of readout channels per branch	29 400
Size of one physics event per FPGA (40 MHz sampling)	24 kbyte
Size of one physics event per branch	35.3 Mbyte
Transfer time of one branch (without overhead)	282 ms

The data of a 'physics event' from one optical module comprise the 20 analog HPD signals that are sampled (using the CERN-SPS 40.0792 MHz frequency as reference clock) and digitised by 8-bit FADCs during two 15 μs long gates (which not only match the two accelerator spills but also allow for the recording of background for 2.5 μs before and after each 10 μs spill). The digitised data are first transferred into a field programmable gate array (FPGA) located inside of each optical module. The next physics trigger follows after a pause of at least 6 s, depending on the SPS running mode. That permits the transmission of the data stored in the 30×49 FPGAs of one branch in a daisy-chained sequence via a single optical fibre link in less than 0.5 s (overhead included) to the surface. The 30 branches transfer their data in parallel to 30 branch DAQ computers located on the surface.

The number of readout channels, the data volume, and transfer times are summarised in Table 5.

The organisation of data transmission builds on the fact that Ethernet packets with embedded IP packets can be created within FPGA logic [48, 49]. The IP packets comprise the event number, data samples proper, trigger code, time stamp, and source and destination addresses. They are transferred from the FPGA to a medium access controller (MAC) chip which assembles the IP packets and transfers them via a duplex pair of optical fibres. The 1470 MACs of one branch are connected to a gigabit router network which provides the source–destination routing.

After storage of all 1470×30 data sets in their respective branch DAQ computers and after event building in the main DAQ computer, the relative time alignment of the data samples from different optical modules must be done. The alignment constants are obtained through peak finding in calibration events using the short pulse of a 1 ns flash light source [50] which is seen simultaneously by the HPDs of several mechanical modules. The flash light source can be moved across the whole detector array, allowing for a time mapping of all mechanical modules. The position of the flash light source can be determined with a precision of ≈ 15 cm with respect to the position of acoustical beacons mounted on the detector array.

Control tasks, as well as the configuration of the MACs and FPGAs and of high- and low-voltage power supplies, are implemented using microprocessors connected via Ethernet to the detector control computer.

The organisation of the front-end electronics, the digitisation, the time stamping, and the readout are schematically shown in Fig. 15.

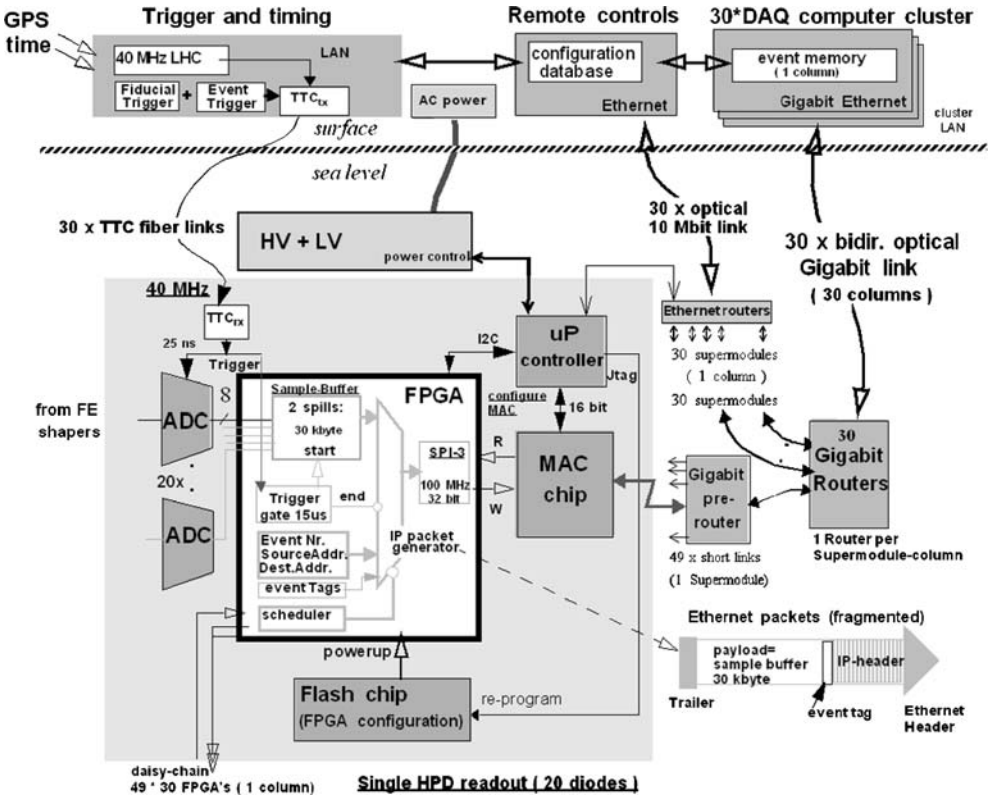

Fig. 15. Electronics diagram of one optical module (*grey-shaded*), and overall readout scheme

6.2.2 Monitoring of light transmission and calibration

The light transmission characteristics of sea water may undergo slight variations with time. The response of the optical modules may also change with time, in particular because of possible sedimentation of particulate pollution on the outer surfaces. Hence additional instrumentation is required to measure these parameters throughout the duration of the experiment.

The measurement of light transmission properties of the sea water is done with a separate device consisting of a set of light diodes emitting at different wavelengths, and light sensors mounted at several, fixed, distances from the light diodes, along the lines pioneered by the ANTARES Collaboration [45], and by the Lake Baikal Collaboration [51]. The device is anchored at the average depth of the main detector. The light diodes are regularly triggered and both the light attenuation length and the light absorption length are determined.

The monitoring of the response of the optical modules of the detector proper is done by using sets of light diodes mounted at the end of a thin pole at a distance of ≈ 10 m from the centre of each mechanical module. In this way each set of light diodes will simultaneously illuminate all 49 optical modules of the mechanical module at angles of incidence smaller than 45°. Additional poles mounted at the four corners of each mechanical module will simultaneously illuminate the optical modules of the four adjacent mechanical modules.

The continuous monitoring of the response of the optical modules permits at the same time the equalisation of their responses, and of the responses of their electronics readout chains, by way of the well discernible amplitude of a single photoelectron signal. This allows for the normalisation of every signal amplitude in terms of the number of photoelectrons.

What is still missing is the effective factor of the conversion to photoelectrons of photons incident on the optical modules. Relative individual fluctuations of the quantum efficiency of the photocathodes of the optical modules, as well as the transmission properties of their transparent surfaces, are calibrated by virtue of the redundancy provided by the illumination of each optical module by several light diode sets. The overall normalisation will be provided by the signal of quasi-elastic CC muon events whose energy is known from the neutrino beam kinematics.

6.3 Mechanical structure

The detector plane is located at a depth of ≈ 1000 m nearly perpendicular to the neutrino beam. The mechanical support structure is anchored to the sea bed during data-taking. It is designed so that it can be moved to different positions in the Gulf of Taranto.

In this section, we describe the detector's mechanical support structure, its deployment and its maintenance.

6.3.1 Conceptual considerations and deployment

Since sea water is corrosive, titanium has been chosen as the metal for the detector's support structure (this metal is also used by the ANTARES and NESTOR Collaborations).

The $300 \times 300\,\mathrm{m}^2$ detector plane is subdivided into mechanical modules of area $10 \times 10\,\mathrm{m}^2$ which are bolted together. The chosen size stems from considerations of construction, transportability, and deployment. Individual mechanical modules are lowered one by one into the water from a vessel. Divers bolt these mechanical modules together to form a row just below the surface of the sea. After the first row of mechanical modules is complete, a mooring system is installed, and the first row is lowered to deeper water to allow for the next row to be bolted to the first row. This process is continued until the full $300 \times 300\,\mathrm{m}^2$ detector plane has been constructed.

The detector is equipped with a robot to extract from the detector plane, and bring to the surface, any mechanical module in order to repair or replace its components.

The mechanical support structure must have sufficient rigidity against water currents. From the point of view of water resistance, the mechanical structure can be imagined as being constructed from a network of titanium tubes of the order of 10 cm diameter holding the optical modules of ≈ 50 cm diameter. Assuming conservatively a maximum water velocity of 10 cm/s and an effective area of 30% of the full square, the calculated total force acting on the detector is ≈ 135 kN. The rigidity of the mechanical structure is achieved by using a tubular truss structure made of three longitudinal titanium tubes of 10 cm diameter that form equilateral triangles. These triangles have a distance of 2 m from each other and are cross-braced for rigidity. Figure 16 shows schematically the structure of a $10 \times 10\,\mathrm{m}^2$ mechanical module together with its 49 optical modules.

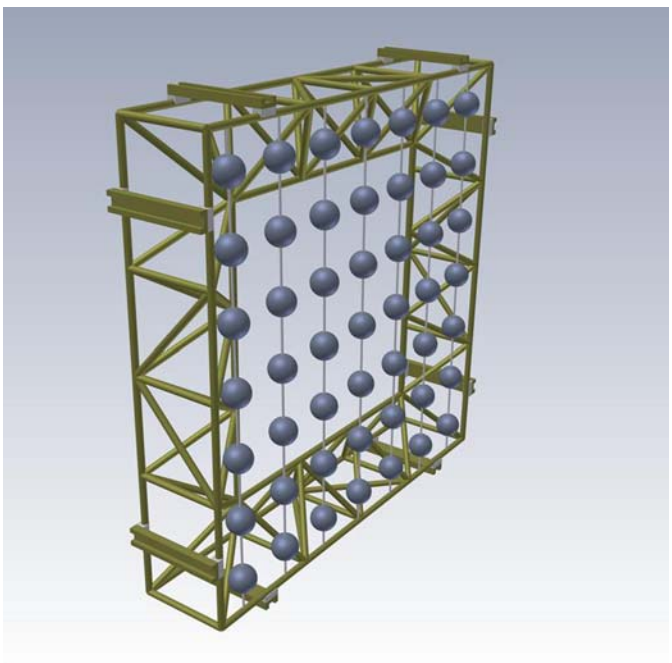

Fig. 16. A $10 \times 10\,\mathrm{m}^2$ mechanical module with optical modules arranged in vertical strings; each side has two guides that locate the mechanical module with respect to the framework located between mechanical modules

The connections between adjacent mechanical modules must be rigid in order to ensure that the 300 m long rows and columns of the detector plane have continuous properties. Analytic and finite element calculations indicate a total weight of the mechanical structure of the order of 5000 t.

All service cables of a mechanical module are directed to the surface. The vertical sides of each mechanical module are equipped with cable trays so that when all mechanical modules are rigidly attached to each other thirty vertical cable trays direct all services to the surface.

A fully equipped mechanical module is buoyant. The up-thrust provided by the 49 optical modules will exceed the weight of the tubing and hence some extra ballast will have to be provided.

The mooring system of the detector plane is shown in Fig. 2. The bifilar system has been adopted to guarantee positional stability of the detector plane. The up-thrust of the two buoys connected to the mooring ropes via pulleys on the detector and on the anchor blocks, which float some 30 m below the sea surface, compensate the up-thrust of the detector plane. The two buoys are connected to the vessel above the detector. In this way the height of the detector array can be changed.

6.3.2 Maintenance

From time to time, elements of the detector will have to be repaired or maintained. Servicing of the electronic components and replacement of optical modules can realistically be done only on the surface. We have adopted the policy that the smallest serviceable unit is a mechanical module.

Using the mooring system, the detector is raised from its working depth of 1000 m up to the servicing position in which the tops of the uppermost mechanical modules are a few metres below the surface of the sea. The service robot is then lowered into the sea and is fixed, by divers, to rails attached to the uppermost mechanical module in the column containing the mechanical module needing to be serviced. The service robot moves down the rail, stops next to the mechanical module that needs to be serviced, is positioned with dowel pins and clamped in place.

With the use of remote handling equipment, the fasteners attaching the mechanical module to its neighbours are released and the mechanical module is pulled out of the plane of the detector and into the service robot.

With the mechanical module securely in place, preparation for the ascent of the service robot to the surface begins. The dowel pins and clamps are released and the robot starts to move. As it goes up a 'finger' releases the mechanical module's cable from its channel. The cable is pulled into the mechanical module and stored (provision has to be made for storing up to 300 m of cable in the mechanical module). When the robot and its contents reach the top of the detector (i.e., opposite the top mechanical module) divers release the service robot from the rails. It can now be raised to the service vessel. Since the cable is attached to the top of the detector, it should be noted that during this final ascent from the top of the detector to the service vessel, cable would be paid out from the service robot.

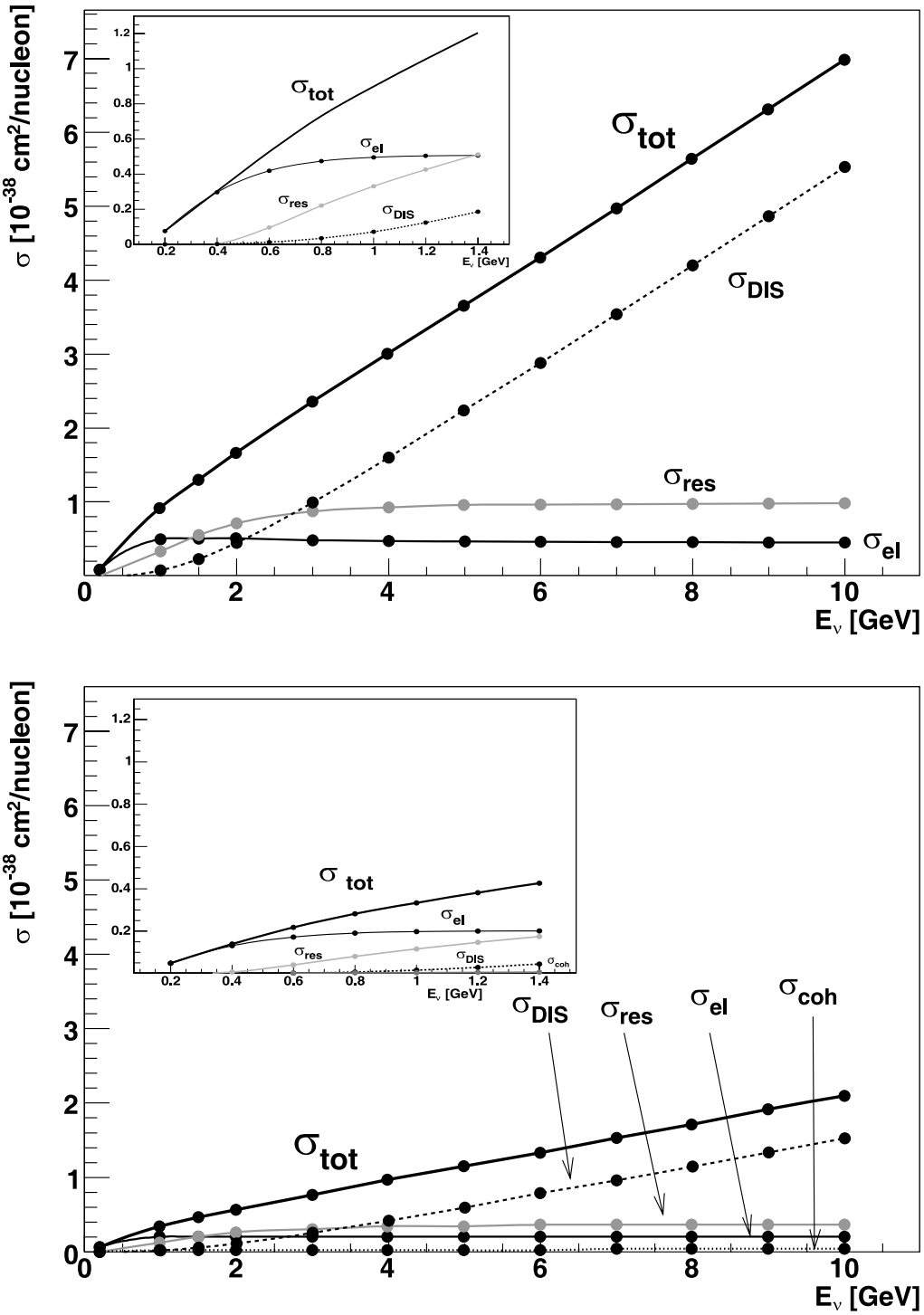

Fig. 17. Charged-current (*top*) and neutral-current (*bottom*) cross-sections per nucleon, as generated by NEUGEN, as a function of the neutrino energy. The subscripts DIS, res, el, and coh refer to the deep-inelastic, resonant, elastic and coherent contributions, respectively. The *inserts* show the region of small neutrino energies, $E_\nu < 1.5$ GeV

7 Event simulation and reconstruction

We have set up a simulation of the experiment based on GEANT4, with a view to simulating the detector response to various types of events, and to evaluating detector properties like resolution of measured physical quantities, signal efficiency and backgrounds. Another goal was to determine important design parameters such as granularity and sensitivity to Cherenkov photons.

7.1 Neutrino cross-sections

Figure 17 shows the cross-sections of various processes as generated by the program NEUGEN[3]. Table 6 lists the CC and NC cross-sections of neutrino–nucleon scattering of 800 MeV neutrinos and antineutrinos, according to NEUGEN.

[3] The program NEUGEN was developed and used in the Soudan-2 and MINOS Collaborations [57].

Table 6. Charged-current and neutral-current cross-sections of neutrino–nucleon scattering of 800 MeV ν_μs and $\overline{\nu}_\mu$s in units of 10^{-38} cm^2/nucleon

	ν_μ	$\overline{\nu}_\mu$
CC total	0.731	0.200
CC quasi-elastic	0.474	0.141
CC resonant	0.221	0.043
CC deep-inelastic	0.035	0.015
NC total	0.282	0.115
NC elastic	0.191	0.082
NC resonant	0.081	0.029
NC deep-inelastic	0.007	0.001
NC coherent	0.003	0.003

We caution that the cross-sections of 800 MeV neutrinos on nucleons are measured only to a precision of 20%. More than 50% of the interactions are quasi-elastic, i.e., the final-state lepton carries nearly the full initial neutrino energy.

7.2 Event generation

Since the aim of the experiment is to measure quasi-elastic events from the interactions of ≈ 800 MeV ν_es and ν_μs, most simulation results will refer to electrons and muons with an average total energy of 800 MeV. Such electrons and muons were generated with a Gaussian fluctuation of the total energy with $\sigma = 80$ MeV, and with a Gaussian angular fluctuation with $\sigma = 170$ mrad around an offset of 100 mrad with respect to perpendicular incidence to the detector plane; this offset takes into account the curvature of the Earth. A sample of π^0s with the same characteristics was also produced.

Figure 18 shows the distribution of the distance of emission of Cherenkov photons from the vertex, for 800 MeV electrons and muons. While the distribution for electrons reflects the shape typical of an electromagnetic shower, the distribution for muons is flat and reflects the muon absorption length in water of ≈ 3.5 m. Therefore, the detector plane will typically see Cherenkov rings with a width of ≈ 3 m.

Table 7. Statistics of Cherenkov photons from 800 MeV electrons and muons

	Electron	Muon
Generated	138 000	104 000
After absorption and scattering	37 500	33 300
Photoelectrons	610	530

The simulation of the measurement of Cherenkov photons in the detector plane proceeds as follows:

- the detector granularity was (for historical reasons) determined by the sum of the responses of a group of four optical modules at the corners of a grid element, i.e., 2.8×2.8 m^2 in area;
- the geometrical photon collection efficiency was taken to be 8% uniformly distributed over this area;
- the resulting number of photons was folded with the quantum efficiency of a bi-alkali photocathode (Fig. 11);
- to the resulting average number of photoelectrons, an average background of 0.1 photoelectrons was added for each group of four optical modules; the resulting sum served as mean value of a Poisson distribution used to generate the observed number of photoelectrons.

Table 7 gives the average numbers of Cherenkov photons for 800 MeV electrons and muons, generated at the interaction vertex and after absorption and scattering for a distance of 20 m between vertex and detector plane. The average number of photoelectrons is also given.

Figure 19 shows the Cherenkov rings in terms of photoelectrons, of a typical electron and muon event with 800 MeV total energy, with the vertex located 20 m upstream of the detector plane. The geometrical 'fuzziness' of electron rings due to showering is evident in comparison with muon rings.

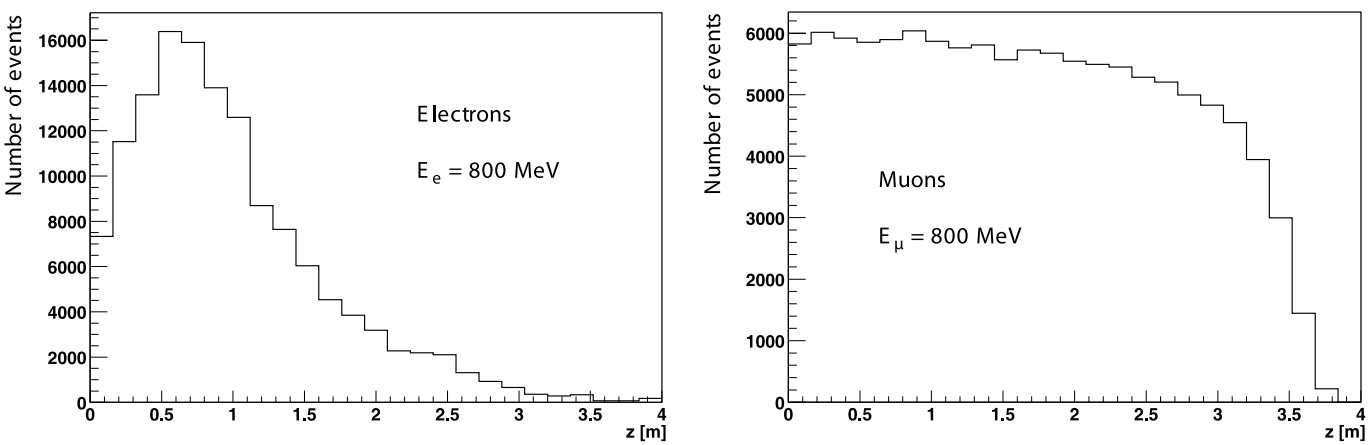

Fig. 18. Distribution of the distance of emission of Cherenkov photons from the vertex, for 800 MeV electrons (*left*) and muons (*right*)

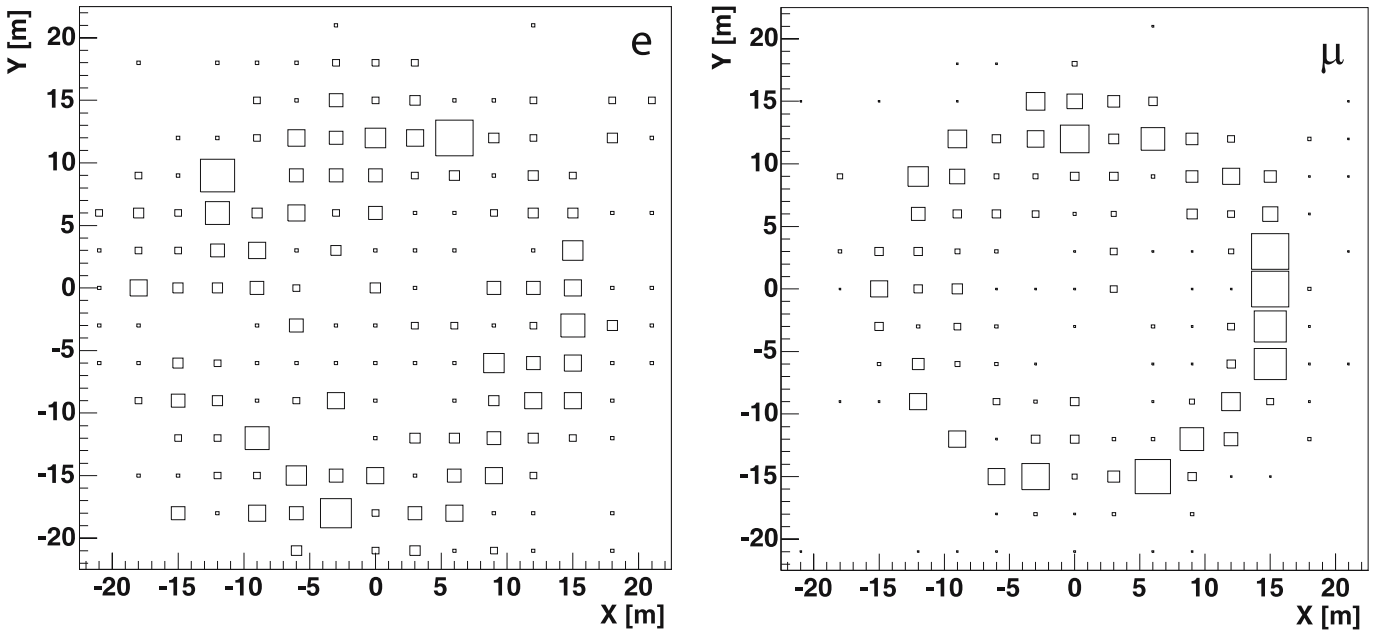

Fig. 19. Cherenkov rings in terms of photoelectrons of a typical electron (*left*) and muon (*right*) event with 800 MeV total energy, with the vertex located 20 m upstream of the detector plane

7.3 Event reconstruction and analysis

The time distribution of the arrival of photons is an important piece of information as it reflects the spatial configuration of the event. Our simulation indicates that a timing resolution of ≤ 2 ns is adequate. Figure 20 shows the average time distribution of 10 electron and 10 muon events, from a vertex located 20 m upstream of the detector plane and with perpendicular incidence on the detector plane, using the arrival of the first photon as time reference.

From the observed time distribution (with a 1 ns binning) and the knowledge of the inverse photon velocity of 4.7 ns/m, it is possible to reconstruct the event vertex without prior knowledge of the event configuration, which is an important asset for event reconstruction. To illustrate this point, and to show the precision of vertex reconstruction in the most imprecise (longitudinal) coordinate, Fig. 21 shows the difference between reconstructed and generated longitudinal vertex coordinate for 800 MeV electrons and muons. A resolution of 1.3 m is achieved.

Knowing the vertex position, the total energy of the event can be reconstructed by correcting the energy observed in each cell by the attenuation due to the known path length of the light. At this step, an average light attenuation length was used that was obtained from a fit of the generated light attenuation for the electron, muon and π^0 samples. After particle identification, the energy

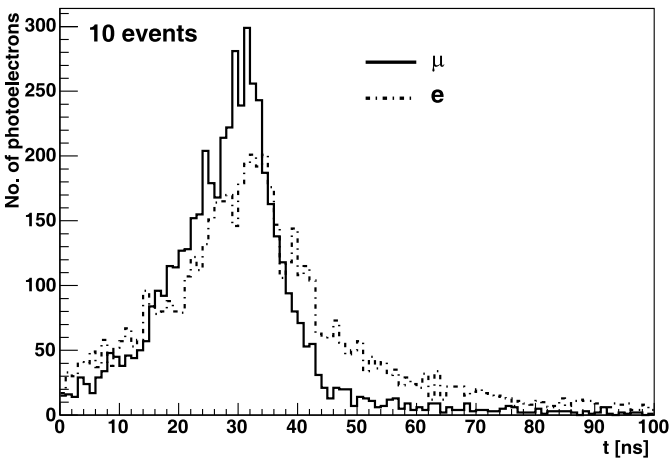

Fig. 20. Time distribution of the arrival of photons from 800 MeV electrons and muons from a vertex located 20 m upstream of the detector plane. The first photon arrives at $t = 0$

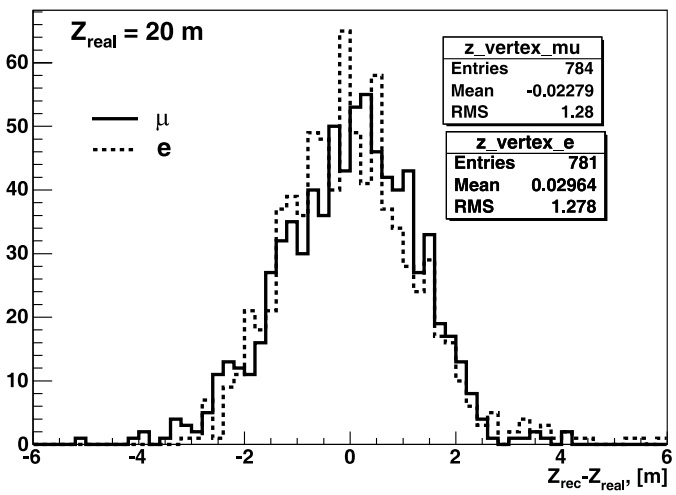

Fig. 21. Difference between reconstructed and generated longitudinal vertex coordinate for 800 MeV electrons and muons

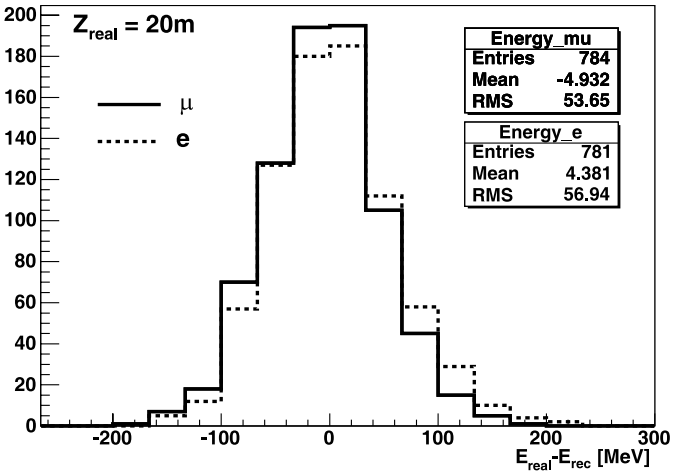

Fig. 22. Energy resolution of 800 MeV electrons and muons

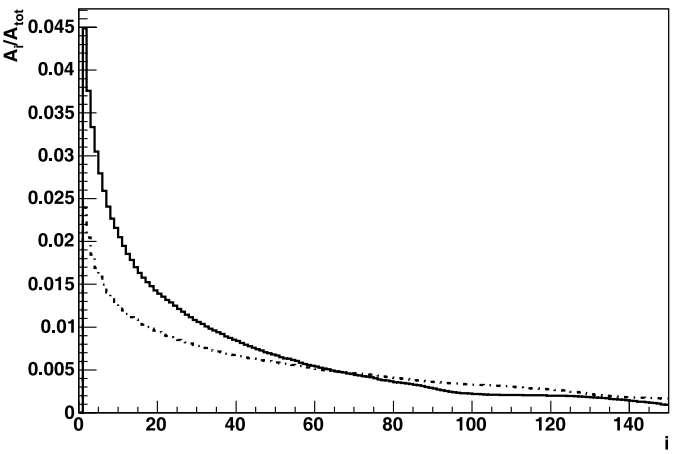

Fig. 23. Average relative energy in the ith non-zero cell when cells are ordered according to their energy content, for 800 MeV electrons (*light*) and muons (*dark*)

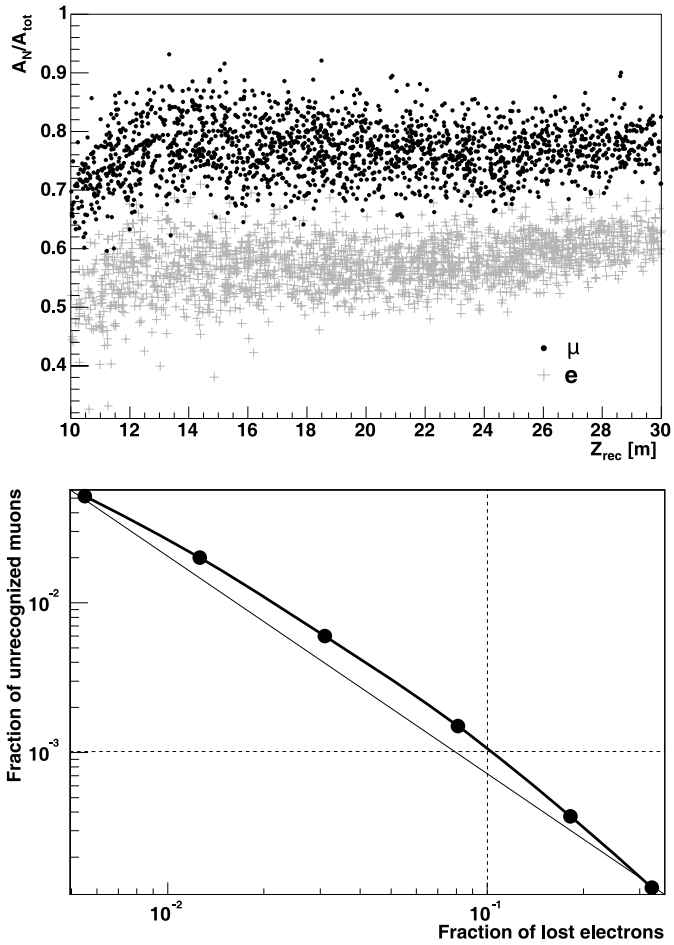

Fig. 24. Separation of 800 MeV electrons and muons as a function of the reconstructed longitudinal vertex position (*top*); muon efficiency versus electron efficiency (*bottom*). The separation is based on amplitude information only

resolution would be improved by applying the appropriate attenuation length. Our procedure thus emulated the one that would be applied in the analysis, i.e. one would optimise the energy resolution after the result of the particle identification. The light attenuation length used at this step varied between 31 and 34 m. Figure 22 shows the resulting difference between reconstructed and true energy. The achieved energy resolution of $\approx 7\%$ is very good and supports a posteriori the choice of Cherenkov light in water as the detection technology.

A key requirement on the detector is its capability to separate electrons from muons, as this is of central importance for sensitivity to a small $\nu_\mu \to \nu_e$ transition probability. In our simulation, we investigated two avenues:

- the 'amplitude' separation which depends on the distribution of amplitudes across all cells, and
- the 'fuzziness' separation which depends on the geometrical configuration of the cells with non-zero hits.

We note here the importance of being sensitive at the one-photoelectron level (which was one motivation of our choice of the HPD as preferred photon detector over a traditional photomultiplier tube).

The amplitude separation rests on the observation that in a 'muon event' the energy is concentrated in fewer cells in comparison to 'electron events'. This is quantified in Fig. 23, which gives the average relative energy in the ith non-zero cell when cells are ordered according to their energy content, for 800 MeV electrons and muons. The separation capability between electrons and muons resulting from the highest relative content in N cells is obvious. A closer inspection confirms what is expected: N will depend on the distance between vertex and detector plane (and may also depend on the level of background photoelectrons).

After optimizing N as a function of the distance between vertex and detector plane, the resulting separation between 800 MeV electrons and muons is shown in Fig. 24 as a function of the longitudinal vertex position (upper plot). The separation capability is satisfactory. Also shown in Fig. 24 is the purity of electrons as a function of their detection efficiency (lower plot): the probability of misidentifying a muon as electron is 1×10^{-3} for a loss of 10% of the electrons.

We note that up to this point the 'fuzziness' separation has not been employed. Since it is based on geometric infor-

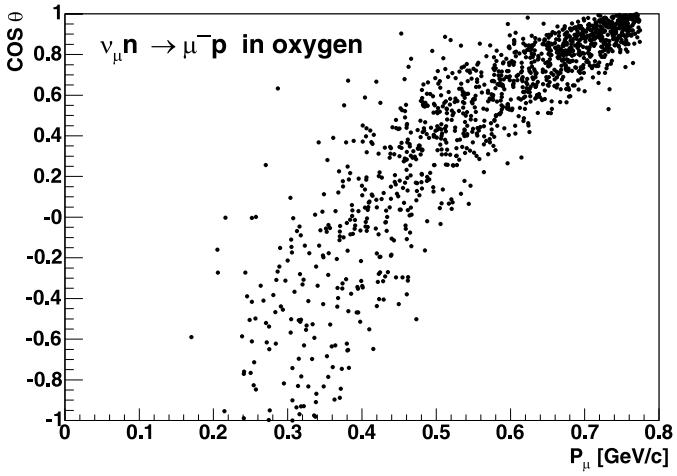

Fig. 25. Cosine of the polar angle of muons from the quasi-elastic reaction in the ^{16}O nucleus versus muon momentum

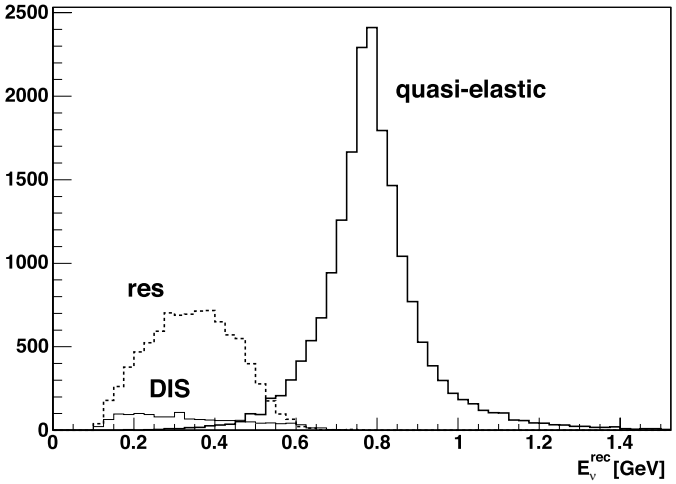

Fig. 26. Neutrino energy reconstructed from events with a single muon under the hypothesis of quasi-elastic neutrino–nucleon scattering

mation, its separation power is largely uncorrelated with that from amplitude information. Thus it will aid the separation of electrons from muons; however, our simulations indicate that its separation power is less powerful than that from amplitude separation.

In our simulation, all neutrino-induced processes were generated with the program NEUGEN. This program incorporates details of low-energy neutrino interactions with nuclei (^{16}O in our case) such as nuclear form factors, Fermi motion, Pauli blocking, and re-interaction of secondary hadrons inside the nucleus. One consequence of this is that the quasi-elastic CC reaction with nucleons inside a nucleus is more complicated than the one with free nucleons: the angular distribution of the outgoing lepton broadens, and the energy distribution becomes asymmetric toward low energy. This is shown in Fig. 25, a scatter plot of the polar angle of muons from the quasi-elastic reaction in the ^{16}O nucleus versus muon momentum.

If all CC reactions (quasi-elastic, resonant π production and deep-inelastic scattering (DIS)) are reconstructed with the kinematic model of quasi-elastic neutrino scattering off a free nucleon, Fig. 26 emerges. It shows the neutrino energy reconstructed from the energy and the polar angle of the final-state lepton. It appears that the quasi-elastic reaction can be well separated from deep-inelastic scattering and resonance production by selecting a lepton energy above ≈ 600 MeV.

After quasi-elastic CC ν_e scattering events are separated from background involving final-state muons, the remaining challenge is their separation from NC-induced events. The most severe background stems from π^0 production in NC interactions, where the π^0 decay into two photons is asymmetric and simulates an isolated forward-going electron.

In NC reactions, π^0s can be produced in deep-inelastic scattering, resonantly off nucleons or coherently off the ^{16}O nucleus (for the cross-sections of these processes, see Table 6 and Fig. 17). For these processes, the correlation of the polar angles of the photons with their momenta

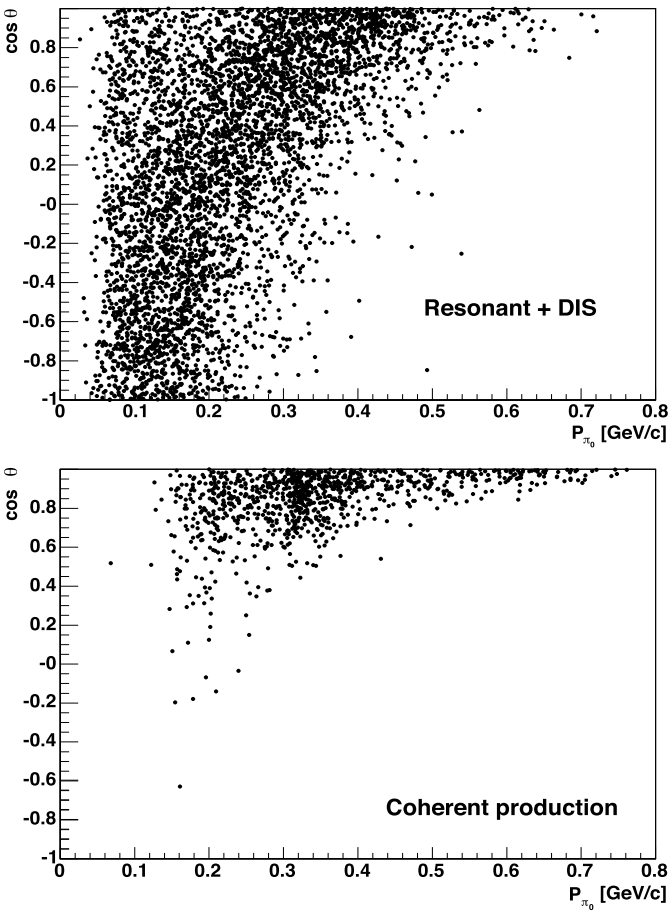

Fig. 27. Cosine of the polar angle versus the photon energy for photons from π^0 production by neutral currents, for ν_μs of 800 MeV: resonant and DIS production (*top*), and coherent production on the ^{16}O nucleus (*bottom*)

are shown in Figs. 27 and 28 for the interactions of 800 MeV and 6 GeV neutrinos, which are typical for ν_μs originating from π^+ and K^+ decays.

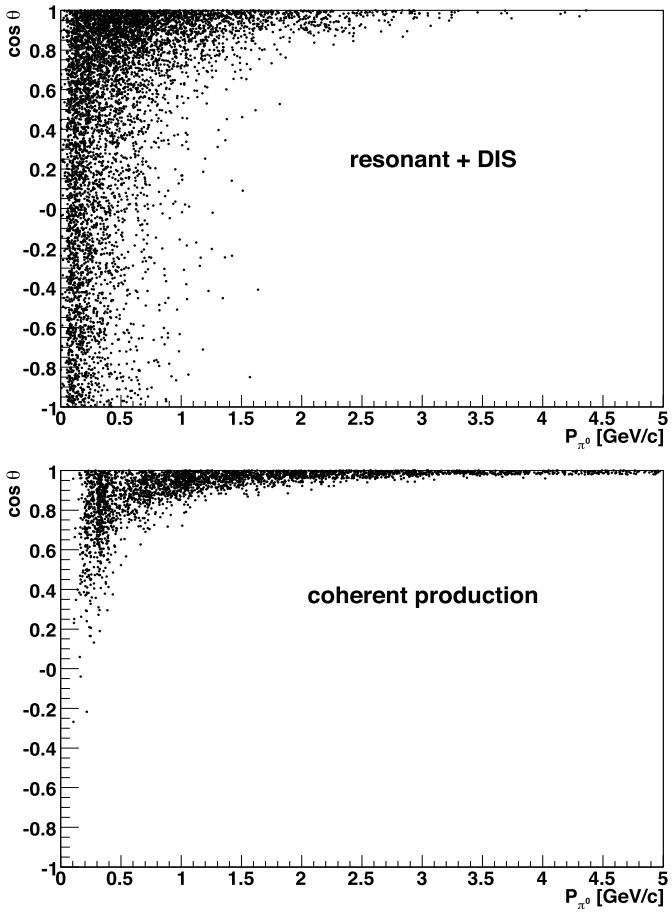

Fig. 28. Cosine of the polar angle versus the photon energy for photons from π^0 production by neutral currents, for ν_μs of 6 GeV: resonant and DIS production (*top*), and coherent production on the ^{16}O nucleus (*bottom*)

Any photon from the decay of such π^0s is considered as background if its energy is between 0.6 and 1.0 GeV and if the other decay photon is either emitted with polar angle larger than 120° or else has an energy smaller than 100 MeV. The resulting photon background is given in Table 8 as a fraction of CC ν_μ events from π^+ decays in the absence of oscillations. The photon background from π^0s originating from NC interactions of ν_μ from K^+ decays is by far dominant. We retain a total of 1.3×10^{-3} for the background estimation.

Table 8. Background of photons from π^0 decays per CC ν_μ event from π^+ decay in the absence of oscillations

	From ν_μ from π^+	From ν_μ from K^+
NC resonant + DIS	0.008×10^{-3}	1.2×10^{-3}
NC coherent	0.012×10^{-3}	0.03×10^{-3}

8 Signals and backgrounds, sensitivity, and comparison with other projects

8.1 Signals and backgrounds

The experiment makes use of two signals: (i) CC quasi-elastic ν_e events with ≈ 800 MeV visible energy, and (ii) CC quasi-elastic ν_μ events with ≈ 800 MeV visible energy.

In the selection of both ν_e and ν_μ signal events, the tails of the off-axis neutrino beam at low and high energy are removed by requiring $0.6\,\text{GeV} < E_\nu^{\text{vis}} < 1.0\,\text{GeV}$. Quasi-elastic events with large polar angles of the outgoing lepton are also removed.

The CC quasi-elastic ν_e sample is further reduced by cuts that suppress the contamination by mis-identified CC quasi-elastic ν_μ events.

Table 9 summarises the signal efficiencies after cuts with respect to the number of quasi-elastic interactions of neutrinos originating from π^+ decays.

Table 10 summarises our estimates of the dominant backgrounds; they are given as percentages of the num-

Table 9. Signal efficiencies after cuts

	CC quasi-elastic ν_e	CC quasi-elastic ν_μ
$0.6\,\text{GeV} < E_\nu^{\text{vis}} < 1.0\,\text{GeV}$	0.9	0.9
Removal of large-angle scattering	0.8	0.8
CC quasi-elastic ν_μ suppression	0.9	–
Overall	0.6	0.7

Table 10. Background percentages w.r.t. the number of CC ν_μ events from π^+ decays in the absence of oscillations

	CC quasi-elastic ν_e (%)	CC quasi-elastic ν_μ (%)
ν_e from K_{e3} and μ decays	0.14	–
Misidentified CC quasi-elastic ν_μ events	0.06	–
Photons from π^0 decays	0.13	–
$\pi^\pm$ from resonant NC production	–	0.1
Sum of background percentages	0.33	0.1

ber of CC ν_μ events from π^+ decays in the absence of oscillations.

There will be a continuous background from ^{40}K decays (an isotope of potassium that is contained in sea salt), and intermittent light from bioluminescence. The ^{40}K background, which consists essentially of single photoelectron signals of order 200 kHz per detector cell [52], translates into a hit probability of 0.02 per 100 ns and poses no problem. Spells of bioluminescence may enforce temporary suspension of data-taking.

No problems arise from cosmic-ray background since the readout is limited to the accelerator spill which gives a reduction by a factor of $\approx 10^5$ with respect to continuous sensitivity.

8.2 Sensitivity to Δm^2_{23} and θ_{23}

Guided by all experimental input available, the experiment will be located at three different positions along the beam, optimally spaced for achieving the best precision on $\sin^2\theta_{23}$ and Δm^2_{23}.

Figure 29 shows the CC quasi-elastic ν_μ rates with and without oscillations, at baselines of 1100, 1200 and

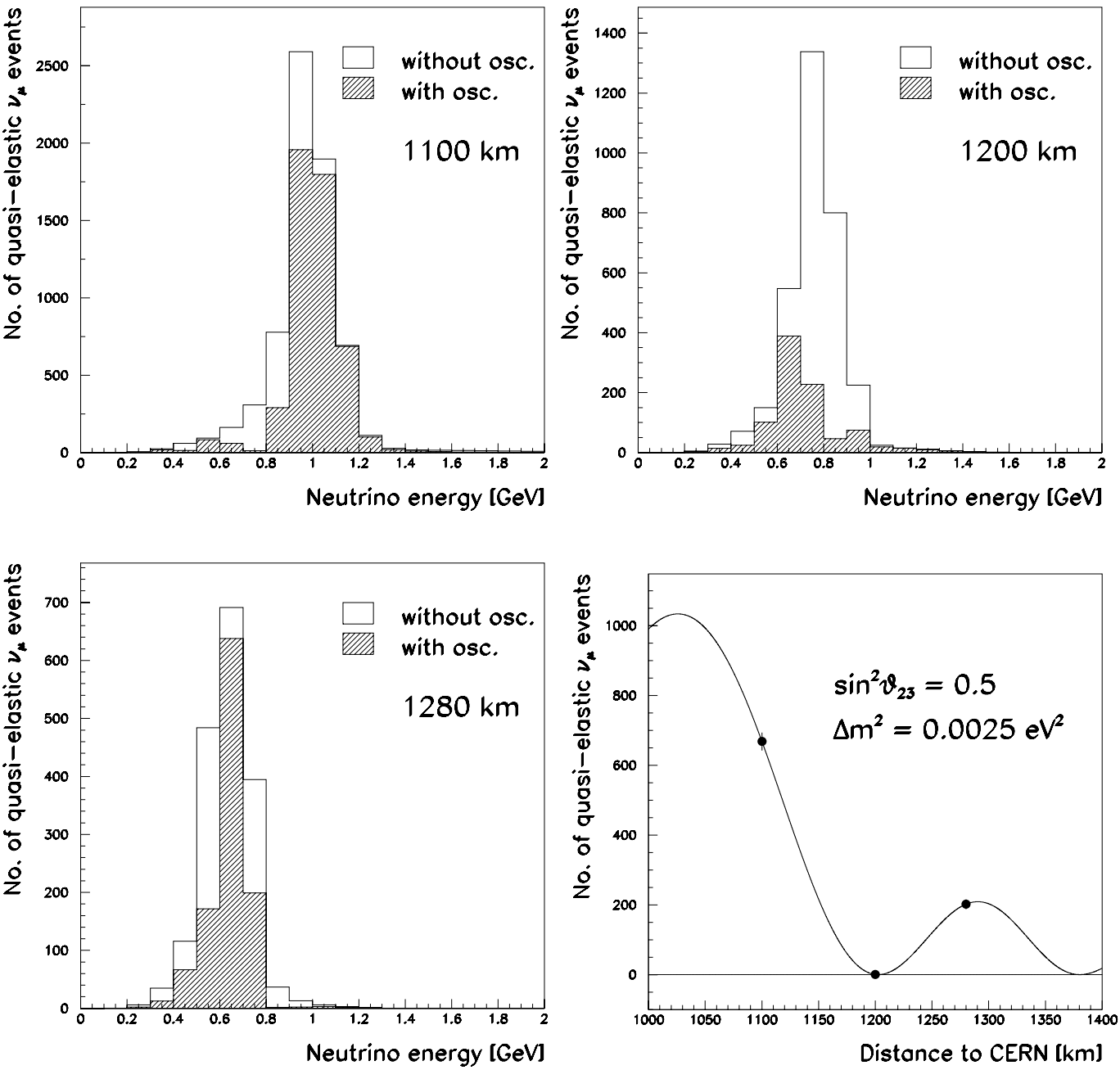

Fig. 29. Charged-current quasi-elastic ν_μ spectra at the three baselines of 1100, 1200 and 1280 km; the *right lower plot* shows a fit of the quasi-elastic event rates in terms of the oscillation parameters $\sin^2\theta_{23}$ and Δm^2_{23}

Table 11. Precision of $\sin^2\theta_{23}$ and Δm^2_{23}

Error on $\sin^2\theta_{23}$	$\approx 6\%$
Error on Δm^2_{23}	$\approx 1\%$

1280 km. The rates take the neutrino fluxes and energies at the different off-axis angles into account. A fit of the rates in terms of $\sin^2\theta_{23}$ and Δm^2_{23} is also shown. There the simplifying assumption of mono-energetic neutrino beams at the three nominal off-axis energies is made. Furthermore, it is assumed that one year of data-taking is spent at either of the 1100 and 1280 km locations, and five years at 1200 km, where the ν_μ rate is close to zero at the nominal off-axis energy. The relative normalisation between the event numbers at the three locations is obtained from the muon flux in the shield after the decay tunnel at CERN, the statistical error of which is negligible compared to the event statistics.

Table 11 gives the numerical results for the errors of the fit parameters. Whilst the precision on $\sin^2\theta_{23}$ is modest, Δm^2_{23} is measured with excellent precision. We stress that the precision of these two parameters stems solely from the rates at the three locations, i.e., additional information from the shape of the energy spectrum has not been used.

Early information from the three positions will define the exact position required for five years of data-taking with maximum sensitivity to the $\nu_\mu \to \nu_e$ transition.

8.3 Sensitivity to θ_{13}

Table 12 gives a summary of the relevant parameters and expected results from the five-year data-taking at the second ν_μ oscillation maximum. The limits given include our estimate of the systematic experimental error.

We wish to stress that the direct experimental result is the transition probability $P(\nu_\mu \to \nu_e)$ at the second oscillation maximum. While the number of ν_e signal events is measured in the longtime-exposure at this oscillation maximum, the number of ν_μ events without oscillation must be inferred from the measurements at all three locations.

In Table 12, this transition probability has been converted into $\sin^2\theta_{13}$ using the MNS mixing matrix of (1) with the following reference set of oscillation parameters: $\Delta m^2_{23} = 2.5\times10^{-3}\,\mathrm{eV}^2$, $\sin^2\theta_{23} = 0.5$, $\Delta m^2_{12} = 8\times10^{-5}\,\mathrm{eV}^2$, CP phase angle $\delta = 0°$, 'normal' mass hierarchy and inclusion of the matter effect. A more detailed analysis which addresses the interplay between θ_{13} and δ, and the influence of the mass hierarchy, is discussed below.

In Fig. 30 we show the number of quasi-elastic ν_e events as a function of the distance from CERN, scaled to the nominal distance of 1200 km. The reference set of oscillation parameters has been used, with the following exceptions: $\sin^2\theta_{13} = 0.003$, CP phase angles 45° and 225°, and both normal and inverted mass hierarchy, respectively. The ν_e events from oscillations are shown on top of the constant background of 15.6 events (Table 12). Whilst the matter effect amounts to a 2% change only, and the dependence on the mass hierarchy is weak, the number of ν_e events from oscillations depends significantly on the choice of θ_{13} and the CP phase angle δ.

Table 13 gives the expected number of quasi-elastic ν_e events at 1200 km, for various sets of oscillation parameters. We note that, even for $\theta_{13} = 0$, the ν_μ–ν_e transition probability is non-zero due to the solar term, resulting in 17.7 $\nu_\mu \to \nu_e$ events.

Figure 31 shows the 90% CL and 3σ limits on $\sin^2\theta_{13}$ as a function of the CP phase angle, for normal and inverted mass hierarchies. For the calculation of the limits, a systematic error of 20% of the estimated number of background events was added quadratically to the statistical

Table 12. Summary of C2GT parameters and expected results from five years of running at the second ν_μ oscillation maximum in search of $\nu_\mu \to \nu_e$ transitions

Radius of instrumented detector disc [m]	150
Height of cone of fiducial volume [m]	20
Fiducial mass [Mt]	1.5
No. of 400 GeV/c protons per year on target	5×10^{19}
No. of useful π^+ decays per proton on target	≈ 0.7
Years of running at oscillation maximum	5
No. of ν_μ CC interactions (w/o osc.)	4731
No. of ν_μ CC quasi-elastic interactions (w/o osc.)	3068
CC quasi-elastic ν_μ selection efficiency	0.7
No. of CC quasi-elastic ν_μ events after cuts (w/o osc.)	2147
CC quasi-elastic ν_e selection efficiency	0.6
No. of background events for the ν_e signal	15.6
Systematic error on background events	20%
Discovery potential (3σ) on $P(\nu_\mu \to \nu_e)$	0.0082
Discovery potential (3σ) on $\sin^2\theta_{13}$ (for $\delta = 0°$ and normal hierarchy)	0.0047
Upper limit (90% CL) on $P(\nu_\mu \to \nu_e)$	0.0035
Upper limit (90% CL) on $\sin^2 2\theta_{13}$ (for $\delta = 0°$ and normal hierarchy)	0.0076
Upper limit (90% CL) on $\sin^2\theta_{13}$ (for $\delta = 0°$ and normal hierarchy)	0.0019

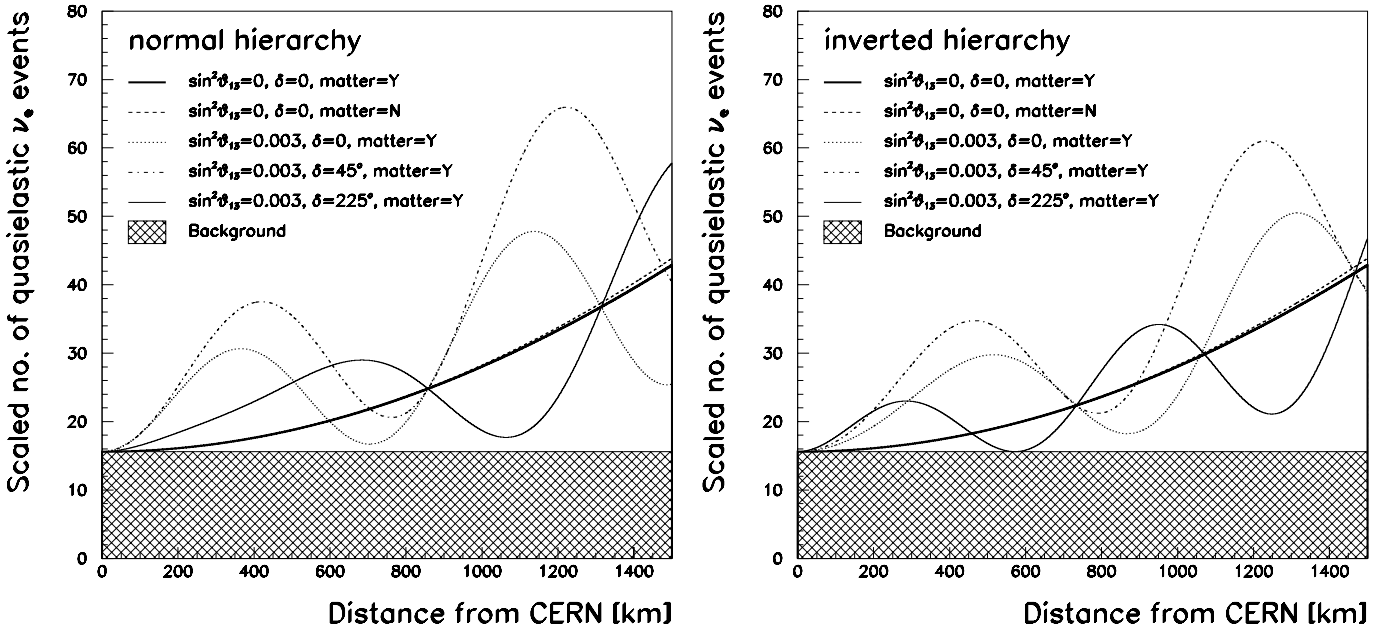

Fig. 30. Charged-current quasi-elastic ν_e event numbers as a function of the distance from CERN, scaled to the nominal distance of 1200 km; event numbers for various sets of oscillation parameters are shown, for normal mass hierarchy (*left plot*) and for inverted hierarchy (*right plot*)

Table 13. Expected number of quasi-elastic ν_e events at 1200 km, for various sets of oscillation parameters; common parameters are $\Delta m^2_{23} = 2.5 \times 10^{-3}$ eV^2, $\sin^2\theta_{23} = 0.5$, and $\Delta m^2_{12} = 8 \times 10^{-5}$ eV^2

$\sin^2\theta_{13}$	CP phase δ [deg]	Hierarchy	Matter effect	No. of events
0	0	normal	yes	17.7
0	0	inverted	yes	17.7
0	0	normal	no	18.1
0	0	inverted	no	18.1
0.003	0	normal	yes	30.6
0.003	0	inverted	yes	29.4
0.003	45	normal	yes	50.1
0.003	45	inverted	yes	44.9
0.003	225	normal	yes	7.9
0.003	225	inverted	yes	6.5
Background				15.6

error from the expected number of quasi-elastic ν_e events from oscillations and from the background of 15.6 events. The shown limits refer to the position in the δ–$\sin^2\theta_{13}$ plane where the null hypothesis of $\sin^2\theta_{13} = 0$ would be ruled out with probability 90% and 99.86%, respectively.

The figure underlines that the C2GT experiment indeed determines, from the experimental measurement of the transition probability $P(\nu_\mu \to \nu_e)$, the *combined* effect from θ_{13}, CP phase angle δ, and the mass hierarchy. Depending on δ, the 90% confidence limit on $\sin^2\theta_{13}$ varies between 0.0002 and 0.023 for normal mass hierarchy, and between 0.0003 and 0.032 for inverted mass hierarchy. Obviously, only a combination with the results of other experiments with different neutrino energies and baselines will allow us to disentangle the effects from θ_{13}, CP violation, and mass hierarchy.

The C2GT experiment, operated with neutrinos only, has practically no sensitivity on the mass hierarchy. Figure 32 shows the region in the δ–$\sin^2\theta_{13}$ plane where the probability of assigning the correct mass hierarchy is at least 90%, but on the assumption that δ and $\sin^2\theta_{13}$ are already precisely known. A significant enhancement of the sensitivity on the mass hierarchy would require running with an antineutrino beam, too.

8.4 Comparison with other projects

The most advanced competing project is T2K [53] in Japan which will send a neutrino beam from the new 50 GeV/c proton synchrotron at J-PARC, under construction, to the refurbished 50 kt Super-Kamiokande detector. It will use

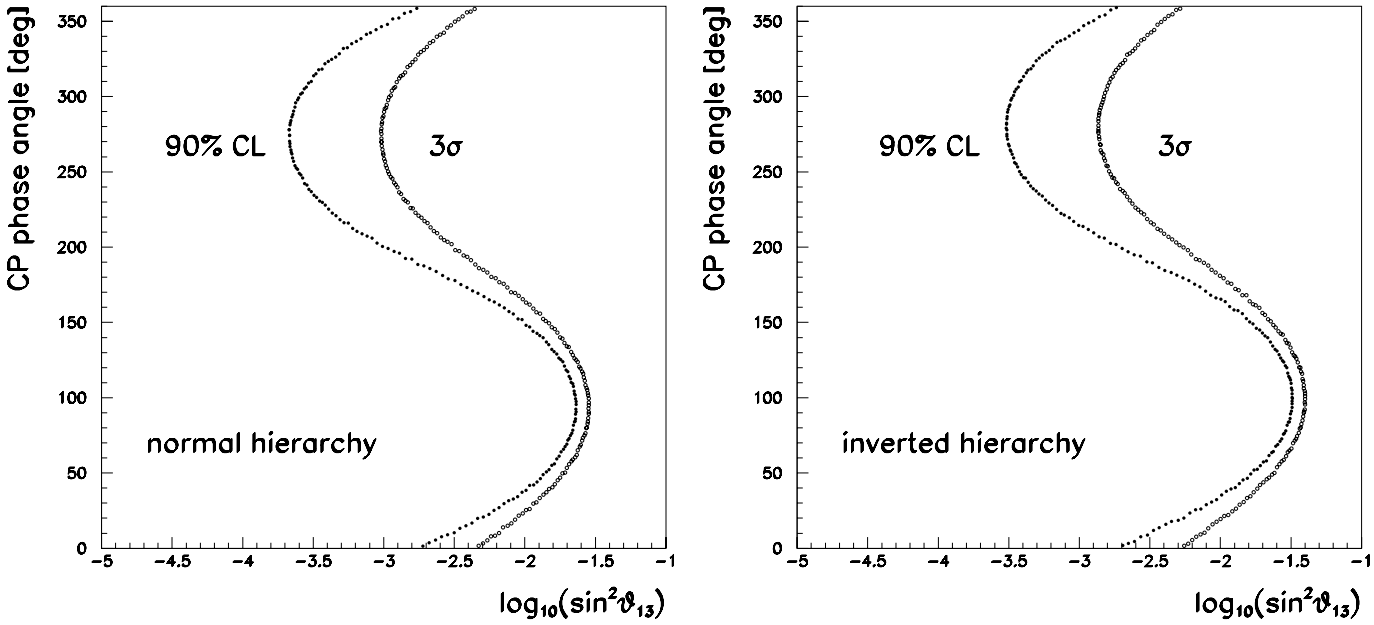

Fig. 31. 90% CL and 3σ limits on $\sin^2\theta_{13}$ as a function of the CP phase angle, for normal (*left plot*) and inverted (*right plot*) mass hierarchy

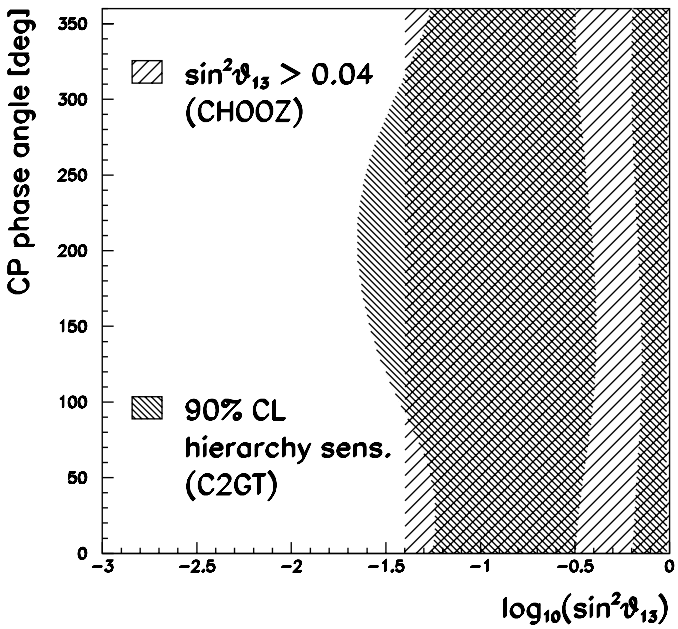

Fig. 32. 90% confidence level region on the mass hierarchy

the off-axis technique to select the right momentum band to be at oscillation maximum. Present planning will have it ready in 2009.

Based on a five-year 'Phase 1' run they estimate a precision on $\sin^2\theta_{23}$ of 1%, and a precision on Δm^2_{23} of 1.3%. As for the measurement of θ_{13}, they expect an average upper limit of 0.0015 at 90% CL on $\sin^2\theta_{13}$, and an average 3σ discovery limit of 0.0040.

The NOνA project [54, 55] at Fermilab also uses the off-axis technique. It will use the NuMI beam and proposes to build a new detector of 30 kt mass at 810 km from Fermilab in the direction of the Soudan mine used by MINOS. A longer baseline, a higher energy, and the use of antineutrinos as well as of neutrinos makes it more suitable than C2GT and T2K to study the mass hierarchy. NOνA quote with 'Phase 1' running conditions for CP phase $\delta = 0$ a 3σ discovery limit of 0.0020 on $\sin^2\theta_{13}$.

Reactor experiments can also measure θ_{13}, as done by CHOOZ. Several projects are being discussed, the most advanced one being double-CHOOZ [56], using two detectors simultaneously; a far detector in the old CHOOZ cavern, and a near one, with a view to reducing systematic neutrino flux uncertainties. Reactor experiments measure θ_{13} with no ambiguities. The double-CHOOZ upper limit on $\sin^2\theta_{13}$ is 0.006 at 90% CL for a five-year run.

9 Summary and conclusions

We have discussed an experiment which exploits a suitably located deep-water trench in the Gulf of Taranto aligned with the CNGS beam, and the possibility of a nearly monochromatic 800 MeV neutrino beam in the off-axis configuration. This permits the use of a moveable underwater detector which, when positioned at three different distances from CERN, will result in an experiment with a strong sensitivity to neutrino oscillation parameters.

The envisaged detector is a water Cherenkov detector at a depth of 1000 m. It has a fiducial mass of 1.5 Mt. The light-detecting elements are located on a disc with radius 150 m, oriented perpendicularly to the neutrino beam.

The experiment confirms unambiguously the oscillatory pattern, neutrino flavour transitions, measures the atmospheric oscillation parameters $\sin^2\theta_{23}$ with modest and

Δm^2_{23} with excellent precision, and is sensitive to a value of θ_{13} much smaller than the current upper limit.

The experiment uses instrumentation which is largely understood, thanks to the pioneering R&D work first of DUMAND, then of the Lake Baikal Collaboration, ANTARES, NEMO and NESTOR.

Overall, the experiment appears both worth while and feasible. The key experimental challenges are (i) the highest possible neutrino flux, (ii) maximal efficiency of collecting Cherenkov light in water, and (iii) maximal reduction of background events which fake CC quasi-elastic ν_e events with 800 MeV energy.

Acknowledgements. We have received much friendly expert advice from members of the NEMO and NESTOR Collaborations, and especially the ANTARES Collaboration. We are indebted to S. Parke, A. Broncano and O. Mena who provided programs for the calculation of neutrino oscillation probabilities. The latter two have also contributed to early conceptual studies. We also thank F. Pietropaolo who contributed to early beam design studies, and P. Sala for her help with the FLUKA program.

References

1. Super-Kamiokande Collaboration, Y. Fukuda et al., Phys. Rev. Lett. **81**, 1562 (1998)
2. Super-Kamiokande Collaboration, Y. Fukuda et al., Phys. Lett. B **433**, 9 (1998)
3. Super-Kamiokande Collaboration, Y. Fukuda et al., Phys. Lett. B **436**, 33 (1998)
4. Super-Kamiokande Collaboration, Y. Ashie et al., Phys. Rev. D **71**, 112 005 (2005)
5. Soudan2 Collaboration, E. Peterson et al., Nucl. Phys. B **77**, 111 (1999)
6. Soudan2 Collaboration, W.W. Allison et al., Phys. Lett. B **449**, 137 (1999)
7. MACRO Collaboration, F. Ronga et al., Nucl. Phys. B **77**, 117 (1999)
8. Y. Suzuki, Accelerator and atmospheric neutrinos – present results. Talk presented at XXIInd Int. Symp. on Lepton–Photon Interactions at High Energy, Uppsala, Sweden, 30 June–5 July, 2004
9. K2K Collaboration, M.H. Ahn et al., Phys. Rev. Lett. **90**, 041 801 (2003)
10. K2K Collaboration, E. Aliu et al., Phys. Rev. Lett. **94**, 081 802 (2005)
11. KamLAND Collaboration, K. Eguchi et al., Phys. Rev. Lett. **90**, 021 802 (2003)
12. KamLAND Collaboration, T. Araki et al., Phys. Rev. Lett. **94**, 081 801 (2005)
13. R. Davis et al., Phys. Rev. Lett. **20**, 1205 (1968)
14. B.T. Cleveland et al., Astrophys. J. **496**, 505 (1998)
15. K. Lande et al., Nucl. Phys. B **77**, 13 (1999)
16. GNO Collaboration, T. Kirsten et al., Nucl. Phys. B **77**, 26 (1999)
17. Kamiokande Collaboration, Y. Fukuda et al., Phys. Rev. Lett. **77**, 1683 (1996)
18. SAGE Collaboration, J.N. Abdurashitov et al., Nucl. Phys. B **77**, 20 (1999)
19. Super-Kamiokande Collaboration, Y. Fukuda et al., Phys. Rev. Lett. **82**, 1810 (1999)
20. Super-Kamiokande Collaboration, J. Hosaka et al., hep-ex/0508053
21. SNO Collaboration, Q.R. Ahmad et al., Phys. Rev. Lett. **87**, 071 301 (2001)
22. SNO Collaboration, Q.R. Ahmad et al., Phys. Rev. Lett. **89**, 011 301 (2002)
23. SNO Collaboration, S.N. Ahmed et al., Phys. Rev. Lett. **92**, 181 301 (2004)
24. SNO Collaboration, B. Aharmim et al., Phys. Rev. C **72**, 055 502 (2005)
25. Z. Maki, M. Nakagawa, S. Sakata, Prog. Theor. Phys. **28**, 970 (1962)
26. Particle Data Group, S. Eidelman et al., Phys. Lett. B **592**, 1 (2004)
27. G. Acquistapace et al., The CERN Neutrino Beam to Gran Sasso (NGS), Report CERN 98–02 and INFN/AE-98/05
28. G. Acquistapace et al., The CERN Neutrino Beam to Gran Sasso (NGS) Addendum CERN SL-99-034 DI and INFN/AE-99/05
29. S. Goswami, Neutrino oscillations and masses. Talk presented at XXIInd Int. Symp. on Lepton–Photon Interactions at High Energy, Uppsala, Sweden, June 30–July 5, 2004
30. M. Apollonio et al., Phys. Lett. B **466**, 415 (1999)
31. M. Apollonio et al., Eur. Phys. J. C **27**, 331 (2003)
32. C. Athanassopoulos et al., Phys. Rev. Lett. **77**, 3082 (1996)
33. A. Aguilar et al., Phys. Rev. D **64**, 112 007 (2001)
34. M. Thomson, Proc. of the XXIst Int. Conf. on Neutrino Physics and Astrophysics, Paris, France, Nucl. Phys. B **143**, 249 (2005) [Proc. Suppl.]
35. D. Autiero, Proc. of the XXIst Int. Conf. on Neutrino Physics and Astrophysics, Paris, France, Nucl. Phys. B **143**, 257 (2005) [Proc. Suppl.]
36. A. De Rújula, M.B. Gavela, P. Hernández, Nucl. Phys. B **547**, 21 (1999)
37. A.K. Mann, in: Proc. of the 3rd NESTOR International Workshop, Pylos, Greece, ed. by L.K. Resvanis (1993) p. 385
38. R.L. Helmer, in: Proc. of the 9th Lake Louise Winter Institute, Lake Louise, Canada, 1994, ed. by A. Astbury et al. (World Scientific, 1995) p. 291
39. D. Beavis et al., Long Baseline Neutrino Oscillation Experiment at the AGS (Proposal E889), Physics Design Report BNL 52459 (1995)
40. NEMO Collaboration, E. Migneco et al., NESTOR Collaboration, L.K. Resvanis et al., contributions to the HENAP Report to PANAGIC, 1 July 2002, http://www.nestor.org.gr
41. NEMO Collaboration, A. Capone et al., Nucl. Instrum. Methods Phys. Res. A **487**, 423 (2002)
42. NESTOR Collaboration, E.G. Anassontzis et al., Nucl. Instrum. Methods Phys. Res. A **479**, 439 (2002)
43. L. Cavaleri (Institute of Marine Sciences ISMAR-CNR, Venice, Italy), private communication
44. L. Cavaleri, Adv. Geosci. **2**, 255 (2005)
45. ANTARES Collaboration, J.A. Aguilar et al., Astropart. Phys. **23**, 131 (2005)
46. C. Joram, Nucl. Phys. B **78**, 407 (1999) [Proc. Suppl.]
47. A. Braem et al., Nucl. Instrum. Methods Phys. Res. A **502**, 205 (2003)

48. H. Muller, F. Bal, A. Guirao, Common Gigabit Ethernet interfaces for HLT and L1 trigger links of LHCb, in: Proc. of the 9th Workshop on Electronics for LHC, Amsterdam, 29 September–3 October, 2003, Report CERN-LECC-2003-055, p. 139
49. H. Muller, A. Guirao, F. Bal, X. Tao, HLT and L1T data streams via quad Gigabit Ethernet interfaces, LHCb Note LHCb DAQ 2004-028
50. J.J. Hernandes-Rey, Review of the Time Calibration System of ANTARES, Proc. of the VLVνT Workshop, NIKHEF, Amsterdam, October 5–8, 2003 (http://www.vlvnt.nl)
51. B.K. Lubsandorzhiev et al., LED calibration system of the Lake Baikal neutrino telescope NT-200+, Proc. of the 29th Int. Cosmic Ray Conf., Pune (India), http://icrc2005.tifr.res.in/htm/PAPERS/OG27/rus-vyatchin-Y-abs1-og27-oral.pdf
52. F. Ameli, M. Bonori, F. Massa, Eur. Phys. J. C **25**, 67 (2002)
53. T2K Collaboration, Y. Hayato et al., A next generation long baseline neutrino oscillation experiment, J-PARC Letter of Intent (January 2003), http://neutrino.kek.jp/jhfnu
54. NOνA Collaboration, D.S. Ayres et al., Proposal to build a 30 kiloton off-axis detector to study $\nu_\mu \leftrightarrow \nu_e$ oscillations in the NuMI beamline, Fermilab Proposal P0929 (March 2005), http://www-nova.fnal.gov
55. Corrigendum, ibidem
56. Double-CHOOZ Collaboration, F. Ardellier et al., A search for the mixing angle θ_{13}, Letter of Intent (May 2004) http://doublechooz.in2p3.fr
57. http://minos.phy.tufts.edu/gallag/neugen